České vysoké učení technické v Praze
Fakulta jaderná a fyzikálně inženýrská

Katedra fyziky
Obor: Experimentální jaderná a částicová fyzika

Konstrukce a zprovoznění detektoru FDD

Construction and comissioning of the FDD detector

BAKALÁŘSKÁ PRÁCE

Vypracoval: Vojtěch Zabloudil
Vedoucí práce: prof. Jesús Guillermo Contreras Nuño, Ph.D.
Rok: 2021

ČESKÉ VYSOKÉ UČENÍ TECHNICKÉ V PRAZE
FAKULTA JADERNÁ A FYZIKÁLNĚ INŽENÝRSKÁ
PRAHA 1 - STARÉ MĚSTO, BŘEHOVÁ 7 - PSČ 115 19

Katedra: fyziky *Akademický rok:* 2020/2021

ZADÁNÍ BAKALÁŘSKÉ PRÁCE

Student: Vojtěch Zabloudil

Studijní program: Aplikace přírodních věd

Obor: Experimentální jaderná a částicová fyzika

Název práce: (česky) Konstrukce a zprovoznění detektoru FDD

Název práce: (anglicky) Construction and comissioning of the FDD detector

Pokyny pro vypracování:

1) Vypracování rešerše na téma:
   - fotoprodukce vektorových mezonů na experimentu ALICE
   - produkce světla v plastových scintilátorech
   - základy fotonásobičů
2) Konstrukce modulů detektoru FDD
3) Určování účinnosti fotonásobičů pro detektor FDD

Doporučená literatura:

[1] J.G. Contreras and J. D. Tapia Takaki: Ultra-peripheral heavy-ion collisions at the LHC, International Journal of Modern Physics A 30(8), 1542012 (2015)

[2] G. F. Knoll: Radiation Detection and Measurement, WILEY (2010)

[3] K. Aamodt, et al. (ALICE Collaboration): The ALICE experiment at the CERN LHC JINST 3 (2008) S08002

Jméno a pracoviště vedoucího bakalářské práce:

prof. Jesus Guillermo Contreras, Ph.D., Katedra fyziky
Fakulta jaderná a fyzikálně inženýrská ČVUT v Praze

Jméno a pracoviště konzultanta:

Solangel Torres Rojas, Ph.D., Katedra fyziky
Fakulta jaderná a fyzikálně inženýrská ČVUT v Praze

Datum zadání bakalářské práce: 23.10.2020

Termín odevzdání bakalářské práce: 07.07.2021

Doba platnosti zadání je dva roky od data zadání.

....
garant oboru

....
vedoucí katedry *děkan*

V Praze dne 23.10.2020

Prohlášení

Prohlašuji, že jsem svou bakalářskou práci vypracoval samostatně a použil jsem pouze podklady (literaturu, software atd.) uvedené v přiloženém seznamu.

Nemám závažný důvod proti použití tohoto školního díla ve smyslu § 60 Zákona č. 121/2000 Sb., o právu autorském, o právech souvisejících s právem autorským a o změně některých zákonů (autorský zákon).

V Praze dne ....

Vojtěch Zabloudil

Acknowledgements

I would like to express my gratitude to my supervisor prof. Jesús Guillermo Contreras Nuño, Ph.D. for his guidance, valuable comments and advices, language corrections, and mainly for his inspiring passion for knowledge. I would also like to thank my consultant Solangel Rojas Torres, Ph.D. for his help, constructive comments and friendly attitude. My thanks goes to my family, particularly to my parents and my girlfriend who always supported me.

Vojtěch Zabloudil

Title:
Construction and comissioning of the FDD detector

Author: Vojtěch Zabloudil

Specialization: Experimental Nuclear and Particle Physics
Sort of project: Bachelor thesis

Supervisor: prof. Jesús Guillermo Contreras Nuño, Ph.D.
Department of Physics, Faculty of Nuclear Sciences and Physical Engineering, Czech Technical University in Prague
Consultant: Solangel Rojas Torres, Ph.D.
Department of Physics, Faculty of Nuclear Sciences and Physical Engineering, Czech Technical University in Prague
Abstract: The ALICE detector is undergoing a major upgrade for Runs 3 and 4 during the Long Shutdown 2. This thesis presents the newly-added Forward Diffractive Detector (FDD) covering forward rapidities. It is made of two layers of plastic scintillators further subdivided into four quadrants. The light from the scintillators is collected at the wavelength-shifting bars located in the sides, which are coupled to a bunch of optical fibres transfering the light to a photomultiplier tube. The main difference of FDD from its predecessor, the AD detector, is the use of much faster materials, the implementation of the laser calibration system and the newly-developed front-end electronics. As FDD covers forward rapidities, it will be useful to tag diffractive processes. It will also help in multiplicity and centrality determination and serve as beam-quality monitor and luminometer. This thesis focuses mainly on the FDD construction and its installation at ALICE.
Key words: trigger, ALICE, scintillator, photomultiplier tube, ultra-peripheral collisions

Název práce:
Konstrukce a zprovoznění detektoru FDD

Autor: Vojtěch Zabloudil

Studijní program: Aplikace přírodních věd
Obor: Experimentální jaderná a částicová fyzika
Druh práce: Bakalářská práce

Vedoucí práce: prof. Jesús Guillermo Contreras Nuño, Ph.D.
Katedra fyziky, Fakulta jaderná a fyzikálně inženýrská, České vysoké učení technické v Praze
Konzultant: Solangel Rojas Torres, Ph.D.
Katedra fyziky, Fakulta jaderná a fyzikálně inženýrská, České vysoké učení technické v Praze
Abstrakt: Detektor ALICE prochází zásadními vylepšeními pro následující běhy 3 a 4 (Run 3 a Run 4) během druhé dlouhé odstávky (Long Shutdown 2). Tato práce představuje nově přidaný Dopředný Difrakční Detektor (FDD) pokrývající dopřednou rapiditu. FDD je vyroben ze dvou vrstev plastových scintilátorů, které jsou dále rozděleny do čtyř kvadrantů. Světlo ze scintilátorů se shromažďuje na proužcích posunuících vlnovou délku, které jsou umístěných po stranách scintilátoru. Proužky jsou spojeny ke svazku optických vláken přenášejících světlo do fotonásobiče. Hlavním rozdílem FDD od jeho předchůdce, detektoru AD, je použití mnohem rychlejších materiálů, implementace laserového kalibračního systému a nově vyvinutá elektronika pro čtení dat. Díky rozšíření dopředné rapidity bude FDD označovat difrakční procesy. Pomůže při určování multiplicity a centrálnosti, bude sloužit také jako luminometr a monitor kvality svazku. Tato práce se zaměřuje především na konstrukci FDD a jeho instalaci na experimentu ALICE.
Klíčová slova: trigger, ALICE, scintilátor, fotonásobič, ultraperiferní srážky

Contents

List of Figures

Introduction

During the Long Shutdown 2 (2019-2020), the ALICE apparatus is undergoing an in-depth upgrade of the set-up. The upgrade reflects the focus of the future ALICE physics programme on rare probes at low transverse momenta, which require improvements in vertexing and tracking efficiency as well as a significant increase of the data-sample size. This thesis is focused on the Forward Diffractive Detector (FDD), a scintillation-based detector for the ALICE system, which is a part of this upgrade.

Chapter 1 brings the introduction to CERN and its Large Hadron Collider (LHC). It presents ALICE as one of the four main experiments at the LHC, its main goals and its layout is discussed. A closer look is given to the upgrade, with the description of its elements, mainly the Fast Interaction Trigger (FIT), which is composed of three detectors, one of them being the FDD.

Chapter 2 provides the opening to particle physics. It discusses the fundamental forces and particles, following with a brief introduction to ultra-peripheral collisions and their purpose at ALICE.

The theoretical background of scintillators and wavelength-shifters is presented in Chapter 3. It includes the division into organic and inorganic scintillators and provides their advantages and disadvantages. The scintillator and wavelength-shifting bars used for FDD are also discussed, with a mention of their properties.

Chapter 4 gives the theoretical introduction to photomultiplier tubes. Their principle and layout is discussed, in particular the dynode structure and its attributes. Fine mesh photomultiplier tubes designed specifically for operation inside large magnetic fields are presented. The FDD photosensor is presented and discussed.

The principal part of this thesis is Chapter 5. It gives detailed instructions for the FDD construction and installation. It includes the lists of needed material as well as the description of the construction processes. The pre-assembly of the detector and the installation of FDD-C in the LHC are also covered.

Chapter 6 describes the characterisation of FDD photomultiplier tubes. The set-up used for the characterisation is shown together with the description of the used components. The data collection is clarified along with the data analysis. A table with the results of individual PMTs is included.

The thesis concludes with a brief summary and an outlook of the future work.

Chapter 1

The ALICE apparatus at the CERN LHC

A brief introduction to the CERN organisation and its Large Hadron Collider is presented in the opening of this chapter, following with a deeper description of the ALICE apparatus with the focus on the upcoming upgrade for Run 3.

1.1 CERN

The European Organization for Nuclear Research (CERN), established in 1954, is a laboratory studying fundamental particles. It is an international collaboration consisting of 23 member states. The facility is located in the Franco-Swiss border near Geneva.

It uses particle accelerators and detectors to study the basic constituents of matter. A beam of particles is accelerated to high energy and then it is made to collide with another beam or a stationary target. The products of these collision are further studied for the purpose of getting new information.

Many key acheivements were obtained at CERN, for example the discovery of the Higgs boson, the first creation of antihydrogen atoms, the invention of the World Wide Web (WWW), and many more.

1.2 The Large Hadron Collider

The Large Hadron Collider (LHC) is the world's largest and the most powerful particle accelerator. It started its journey in 2008 being the latest addition to the accelerator complex of CERN (see Figure 1.1).

The LHC is a 27-kilometre ring consisting of thousands of magnets and a number of accelerating systems boosting the particle energy. Two high-energy particle beams, separated in two beam tubes kept at ultra-high vacuum inside this synchrotron

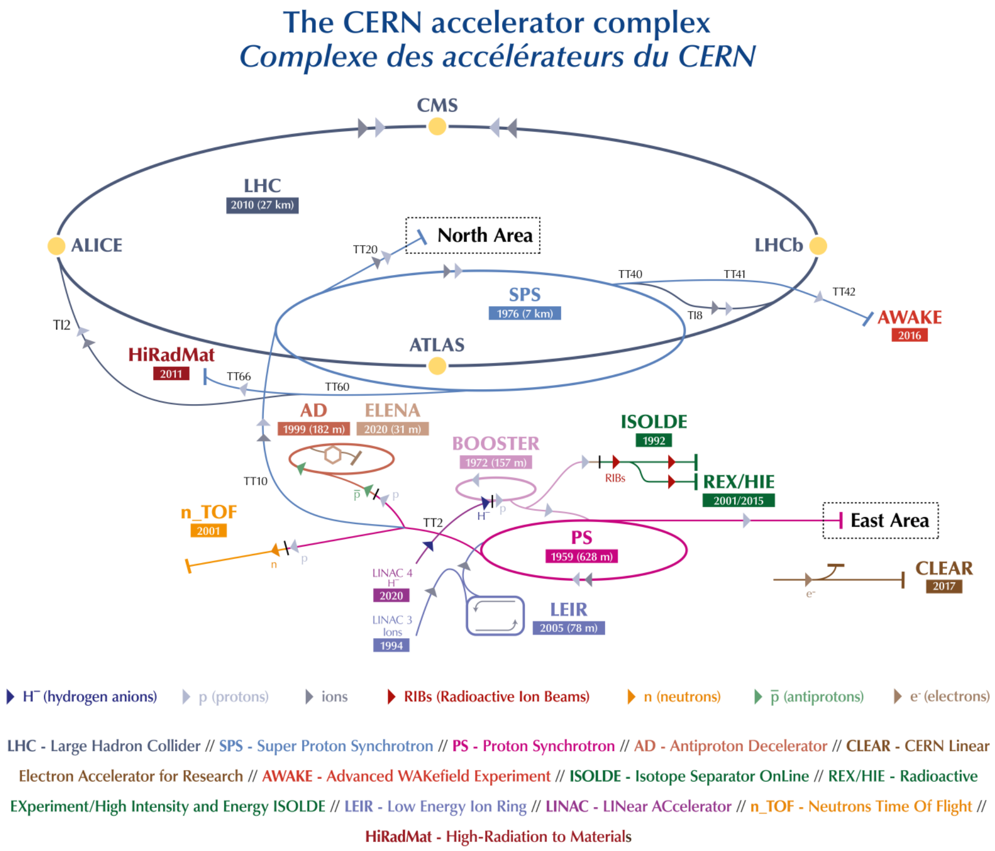

Figure 1.1: The CERN accelerator complex [14].

accelerator, travel at increasing speeds in opposite directions. When the speed of the beams is close to that of light, they are made to collide with one another at four locations corresponding to the particle detectors: ATLAS, CMS, ALICE and LHCb.

To accelerate the proton beam to the energy of 6.5 TeV, it needs to go through an accelerator chain. A hydrogen bottle is used as a source of the protons, which are created by stripping off the electrons from hydrogen gas using an electric field. The created proton beam is initially accelerated by the linear accelerator Linac 2 to an energy of 50 MeV. It is then injected into the Proton Synchrotron Booster (PSB) accelerating the beam to 1.4 GeV. The beam is subsequently accelerated in the Proton Synchrotron (PS) to an energy of 25 GeV, following with the Super Proton Synchrotron (SPS) accelerating the beam to 450 GeV. Finally, the two proton beams are transferred to the LHC beam tubes where they circulate in opposite directions. Up to now, the maximum energy at the collision points in proton–proton collisions is 13 TeV.

For the acceleration of lead ions in the LHC, a slightly different method is used. Vaporized lead is used as a source of ions, which are at first accelerated by the linear accelerator Linac 3. Then they are collected and accelerated in the Low Energy Ion

Ring (LEIR). The beam then continues to the PS and from then onwards follows the same path as the proton beam.

The acceleration in the LHC is caused by radio-frequency cavities (RF). These are metallic chambers containing an electromagnetic field, from which the charged particles receive an electrical impulse to accelerate. The beam is accelerated once per orbit by 8 (16 in total) RF cavities in the LHC. The maximum energy is reached in around 20 minutes and the beam passes through the RF cavities more than 10 million times. To avoid collisions with gas molecules inside the accelerator, the beams are kept in a vacuum as empty as the interstellar space. The LHC uses the largest vacuum system in the world providing a pressure as low as 10^{-11} mbar. There are 1232 15-metre long superconducting dipole magnets, chilled to $-271.3\,^{\circ}$C, keeping the beam on a circular track. Such temperatures are achieved by the world's largest cryogenic system using liquid helium. Another 392 quadrupole magnets with length of 5–7 metres are used to focus the beam [22].

1.3 The ALICE detector

A Large Ion Collider Experiment (ALICE) is one of the four large detectors at the CERN LHC. It is a general-purpose heavy-ion detector with focus on quantum chromodynamics (QCD). LHC has delivered to ALICE proton–proton collisions (pp), proton–nucleus collision and heavy-nuclei collisions (Pb–Pb and Xe–Xe). The latter collisions system allows us to study the quark-gluon plasma (QGP) at extreme conditions, while the others are used to vary the energy density and provide reference data. The structure of the ALICE detector for Run 2 (2015-2018) is shown in Figure 1.2. It consists of a central barrel measuring hadrons, electrons and photons, and a muon arm, located at forward rapidities. The central barrel covers polar angles of 45° to 135° and it is embedded in a large solenoid magnet [3].

1.3.1 Detector layout

The central barrel in Run 2 was comprised of the Inner Tracking System (ITS), Time-Projection Chamber (TPC), Time-of-Flight detector (TOF), Ring Imaging Cherenkov (HMPID), Transition Radiation Detector (TRD) and two calorimeters (EMCal and PHOS) as well as some smaller detectors PMD, FMD, T0 and V0. An array of scintillators (ACORDE), located on the top of the L3 magnet, triggering on cosmic rays, was also included. The AD and ZDC detectors were located at forward rapidities.

The muon spectrometer was included to measure vector mesons via their dimuon decay. For the Run 2, it consisted of the absorber filtering only muons, the muon dipole magnet, the tracking system, and the trigger system.

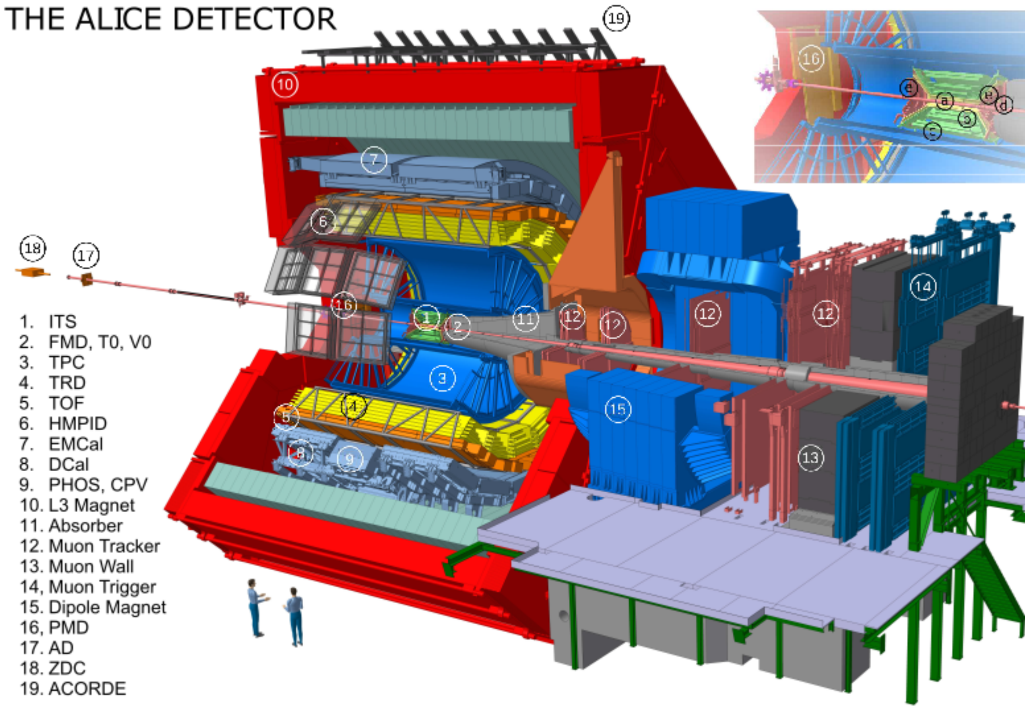

Figure 1.2: A schematic drawing of the ALICE detector for Run 2 [20].

1.4 Upgrade for Run 3

During the Long Shutdown 2, ALICE is undergoing an in-depth upgrade of the set-up. The upgrade reflects the focus of the future ALICE physics programme on rare probes at low transverse momenta, which require improvements in vertexing and tracking efficiency as well as a significant increase in the size of the data sample (corresponding to the increase of the interaction rate), as these observables have very small signal-to-background ratios.

The biggest difference with respect to Run 2 is the increase of the interaction rate up to 50 kHz in Pb-Pb collisions and 1 MHz in pp collisions, which is a rise of two orders of magnitude compared to Run 2. Improvements in data acquisition (DAQ) and computing infrastructure are therefore needed in order to cope with the increased interaction rate. This also compels the majority of ALICE detectors to switch to continuous readout. However, some of the older systems still need an external trigger, which will be provided by The Fast Interaction Trigger further discussed in Ref. [19].

The data processing will provide a reduction factor of 35, which will enable to store the data collected during a Pb-Pb data taking period on a 60 PB buffer disk. The flow of 3.5 TB/s of raw data from the detectors is at first reduced by the First Level Processing (FLP) nodes to ∼600 GB/s. This is further reduced by the Event Processing layer to ∼100 GB/s, which will be stored permanently [24].

The schematic drawing of the upgrade for Run 3 (2022-2024) is shown in Figure 1.3.

It consists of seven main elements:

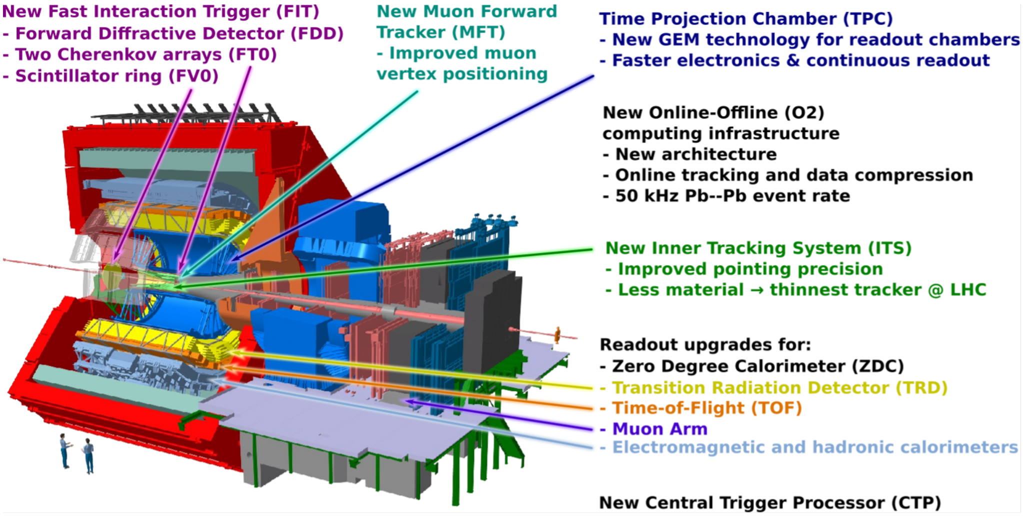

Figure 1.3: The ALICE upgrade for Run 3 [19].

- **Muon Forward Tracker**

  The Muon Forward Tracker (MFT) is a new Si-tracking detector, which is designed to improve muon vertex positioning to the Muon spectrometer. It will provide a way to extend the precision measurements towards the forward rapidities from −3.6 to −2.45 and open the path to new physics not accessible with the detector set-up for Run 2. The MFT uses silicon pixel sensors, which were developed for the ITS and MFT by the ALICE pixel groups. The MFT read-out electronics is the same as for the ITS [21].

- **Time Projection Chamber**

  The increase of the interaction rate requires elimination of the intrinsic trigger rate limit of the original Time Projection Chamber (TPC), which used Multiwire Proportional Chamber (MWPC)-technology. Simultaneously, the excellent momentum and $\mathrm{d}E/\mathrm{d}x$ resolution of the original TPC must be retained. This is possible by the replacement of the MWPC with Gas Electron Multiplier (GEM) detectors, which provide separation of several amplification stages. This allows the drift path of back-drifting ions from subsequent layers to be blocked. The new TPC will use a stack of four GEMs with highly optimised transfer fields between the layers and operating gas mixture. New front-end electronics with continuous readout is included as well [23].

- **Inner Tracking System**

  The upgrade of the Inner Tracking System (ITS) consists of: a new layout combining seven cylindrical layers equipped with ALPIDE Monolithic Active

Pixel Sensors (MAPS) chips, a great material reduction and a reduced distance of the innermost layer to the interaction point. This provides a strong improvement of the tracking efficiency at low transverse momenta and the resolution of the impact parameter. The ITS layout and a table with geometrical details for each layer is shown in Figure 1.4 [9].

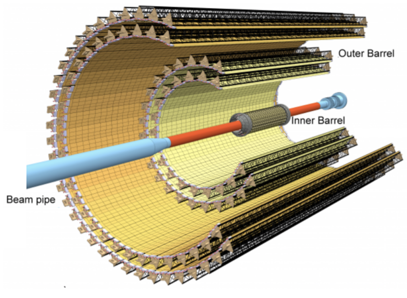

BARREL	LAYERS	RADIUS (cm)	LENGHT (cm)	NUM. STAVES	NUM. CHIPS
Inner	Layer 0	22.4	271	12	108
Inner	Layer 1	30.1	271	16	144
Inner	Layer 2	37.8	271	20	180
Outer	Layer 3	194.4	843	24	2688
Outer	Layer 4	243.9	843	30	3360
Outer	Layer 5	342.3	1475	42	8232
Outer	Layer 6	391.8	1475	48	9408

Figure 1.4: The layout of the upgraded ITS (left) with a table summarizing information about the individual layers and their charachteristics (right) [9].

- **Online-Offline (O^2) system**

The two-order-of-magnitude increase in the data collection achieved in the Runs 3 and 4 is a crucial upgrade of the ALICE system. However, this also implies the growth of the cost and requirements on the computing infrastructure for the data processing and storage. In order to reduce this, the data flow is reduced as close as possible to the readout from the detectors. The ALICE system will use a new Online-Offline (O^2) computing system, which combines the two components together.

For the upcoming runs, the majority of the detectors will be read-out in a continuous mode. The data flow will be chopped into smaller parts called Time Frames by dedicated devices, which use the LHC clock for synchronisation. The reduction of the data volume is carried out by processing the data in parallel with the data collection. After this synchronous process, a final processing step is done asynchronously before permanent storage of the data [8].

- **Readout upgrades**

In addition to the upgrades mentioned above, there are many other readout upgrades of the ALICE detectors, namely of: the Transition Radiation Detector (TRD), the Time Of Flight detector (TOF), the Zero Degree Calorimeter (ZDC), detectors of the muon arm, and hadronic and electromagnetic calorimeters [4].

- **Fast Interaction Trigger**

  The Fast Interaction Trigger (FIT) is a key element added to the ALICE system for Runs 3 and 4. It will provide minimum-bias (MB) trigger for all of the ALICE detectors except TPC. As this thesis focuses on one of the three subsystems of FIT, a more detailed section is devoted to this topic below.

- **Central Trigger Processor**

1.5 Fast Interaction Trigger

The Fast Interaction Trigger consists of three subsystems: FT0, FV0 and FDD (see Figure 1.5), each devoted to different functions and operational regimes. The FT0 is a fast Cherenkov detector array equipped with Micro Channel Plate photomultiplier tubes (MCP-PMT). The FV0 is a scintillator-based detector which functions as a minimum-bias (MB) and centrality trigger, beam-gas background rate monitor as well as a luminometer [19].

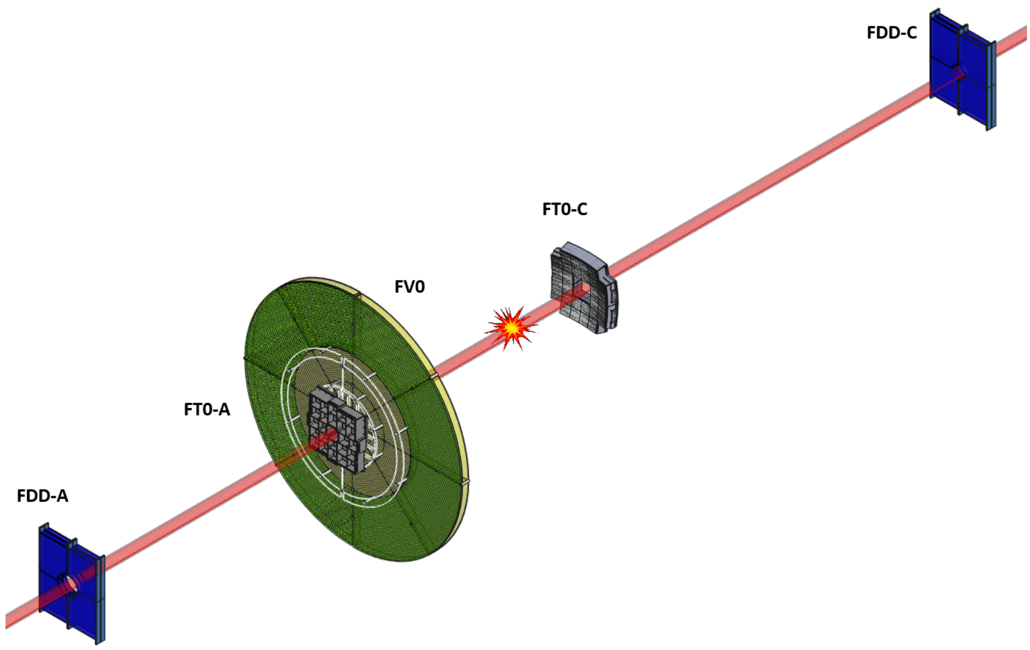

Figure 1.5: The schematic drawing of the Fast Interaction Trigger. From bottom left: FDD-A (blue), FT0-A (grey), FV0 (green), interaction point, FT0-C (grey) and FDD-C (blue). Distances between the detectors are not up to scale [6].

1.5.1 The Forward Diffractive Detector

The Forward Diffractive Detector (FDD) is a scintillation-based detector covering the forward pseudorapidity range. It is divided into two stations: FDD-A and

FDD-C which are located at distances of 17 m and 19.5 m from the interaction point along the beam-line, respectively. The pseudorapidity coverage is from 4.8 to 6.3 for FDD-A and from −7.0 to −4.9 for FDD-C.

The schematic drawing of one FDD station is shown in Figure 1.6. Each station is made of two layers of plastic scintillators further subdivided into four quadrants. For each quadrant, there is a plastic scintillator connected to a pair of wavelength-shifting (WLS) bars that collect the light produced by the scintillator. The light is further transferred via optical fibres to a photomultiplier tube (PMT), where it is converted into the corresponding electrical signal.

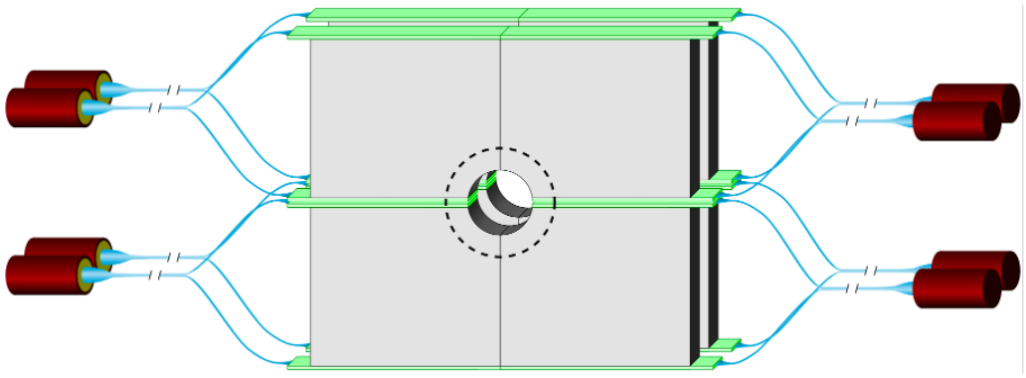

Figure 1.6: Schematic drawing of FDD-C: the plastic pads are shown in grey, the WLS bars in green, the fibre bunches in blue and the PMTs in dark red. The only differences with respect to FDD-A are that the inner hole is larger as depicted by the black dashed line and the length of the fibre bunches [19].

A closer look at the components of FDD is given in the following chapters: Chapter 3 provides information about the materials of the plastics used in FDD and their properties, while Chapter 4 talks about the photomultiplier tubes with focus on fine mesh PMTs used in FDD. Chapter 5 is dedicated to the construction and installation of FDD.

FDD will be used to tag the presence of exclusive diffractive processes by providing a veto on activity at forward rapidities, to tag dissociative diffractive processes by detecting activity in events with rapidity gaps elsewhere. It will also contribute to more technical tasks such as background monitoring using the arrival times of the particles to the detector, centrality, and luminosity determination.

Chapter 2

Ultra-peripheral collisions

While the ALICE detector has been designed to study the properties of the quark-gluon plasma, it is also able to study other aspects of quantum chromodynamics, e.g. the structure of hadrons in terms of quarks and gluons. One key tool for this latter type of study are ultra-peripheral collisions.

This chapter provides basic ideas regarding the proton structure. It explains its basic components through an introduction into the Standard Model. The proton structure is studied through ultra-peripheral collisions, which are further discussed. These collisions include processes extremely sensitive to gluon distributions called vector meson photoproduction, in which the FDD plays an important role.

2.1 The Standard Model

The Standard Model (SM) is a unified theory of quantum chromodynamics and the electroweak interaction. It is the best model to describe our current understanding of how particles and interactions work. Everything in the SM is thought of as quantum fields. Particles are considered as excitations, quanta of these fields, which can interact together. Three of the four fundamental interactions are included in the SM: electromagnetism, the strong force and the weak force. The theory is incomplete due to the absence of a description of quantum gravity, which is a heavily researched topic. However, the lack of quantum gravity does not play a huge role in particle physics as it is extremely weak with respect to the other interactions, making it justifiable to neglect it.

The particles in the SM are divided into two groups according to their spin: **fermions** with half integer spin and **bosons** with integer spin. The SM is often compressed into a diagram, that combines the knowledge presented in this section. The particles are appositely arranged into groups and families. The Standard Model is discussed in the following section. The diagram is shown in Figure 2.1.

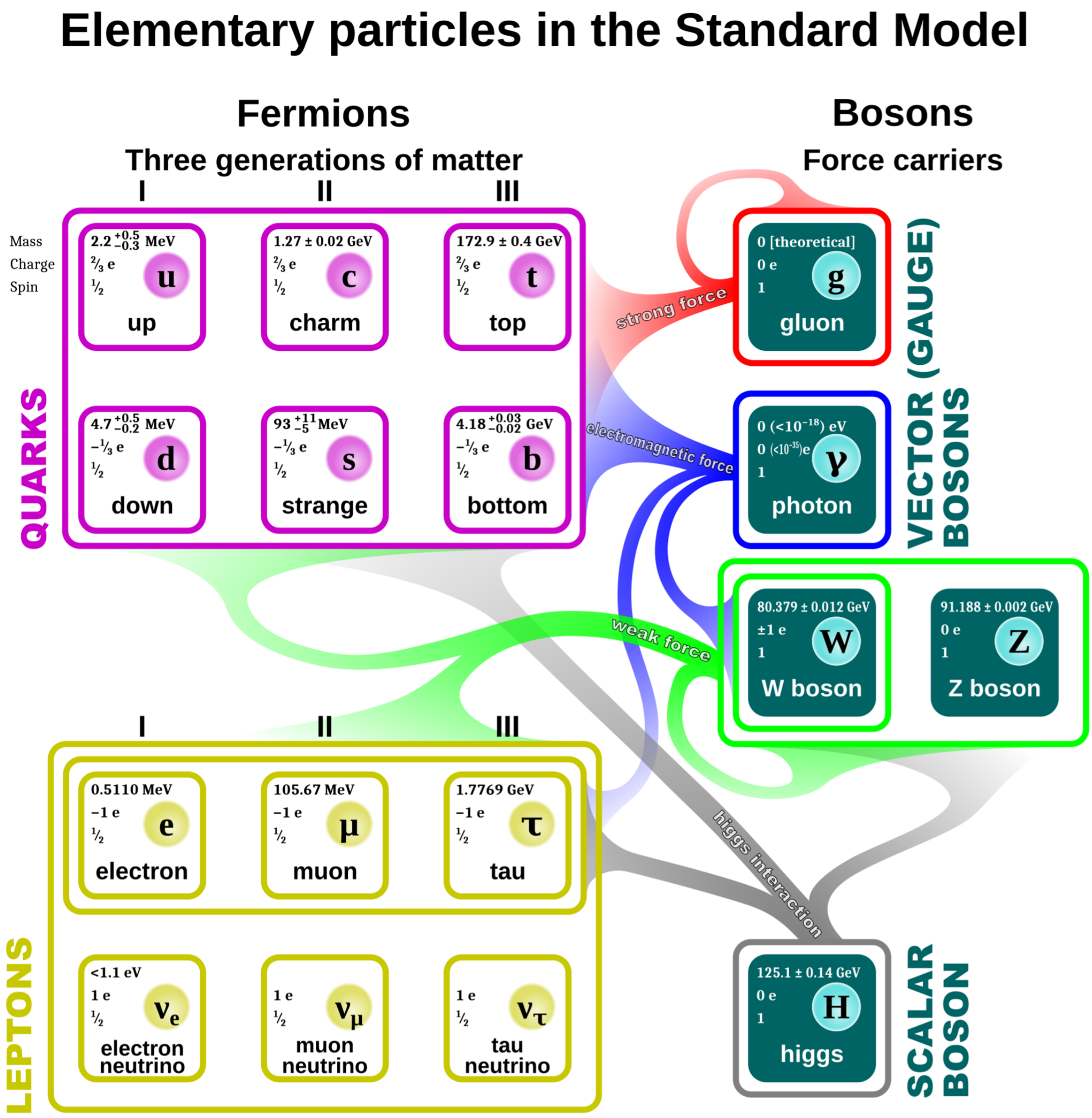

Figure 2.1: Diagram of the Standard Model [19].

2.1.1 Fermions

The SM includes 12 particles known as fermions. They have a spin of 1/2, which causes them to obey the Pauli exclusion principle. Each of them has a corresponding anti-particle, which has the same mass and opposite charge.

Quarks

Quarks are fundamental parts of matter. The six quarks, also called flavours, are: up (u) and down (d), charm (c) and strange (s), top (t) and bottom (b).

They are the only particles with non-integer electric charge, i.e. their electric charge is not an integer multiple of the elementary charge. They have a non-zero colour charge allowing them to interact via the strong interaction. The quantum number of colour charge has three values called red, green and blue. The colour of an anti-particle corresponding to a particle of certain colour is the corresponding anti-colour. The anti-colours are called simply anti-red, anti-green and anti-blue.

Particles can exist on their own only if they are colour neutral, a phenomenon also known as colour confinement. Colour neutrality is achieved by a combination of all of the three colours at once or by a combination of a colour with its corresponding anti-colour. As quarks have a net colour and are therefore unable to exist on their own, they combine together forming colour neutral objects as described earlier. These are called **mesons** containing a quark and an anti-quark and **baryons** composed of three quarks. The examples of mesons are J/ψ, pions or kaons, while the most common baryons are neutrons or protons, whose structure is discussed later in this chapter.

Exotic hadrons containing more valence quarks such as tetraquarks (2 quarks and 2 anti-quarks), pentaquarks (4 quarks and 1 anti-quark) or even higher orders may also exist. Despite the fact that multiple experiments announced their discoveries in recent years, they were still not fully accepted by the physics community.

Leptons

Leptons, same as quarks, are subdivided into three families. The first one is the electron family, which includes the electron (e^-), its anti-particle the positron (e^+). The second family is the muon one, consisting of the muon (μ^-) and the anti-muon (μ^+). The heaviest lepton is the tau lepton which together with the anti-tau forms the tau family.

Each of these families has corresponding neutrinos, which have no electromagnetic charge, hence they interact only through the weak force. Even though the SM states neutrino as massless, neutrinos have an extremely small, non-zero mass. Due to these properties, the neutrino interaction with matter is very rare making them difficult to detect.

2.1.2 Bosons

Bosons are particles responsible for the interactions. Each of the fundamental interactions has a gauge boson with a spin of 1. These are photons, $W^{\pm}$ and Z^0 bosons and gluons, which will be discussed in the following sections.

In the Standard Model, there is also a scalar boson (spin 0) called the Higgs boson. It is the mediator of the Higgs field, which through interactions gives rise to the rest mass of all elementary particles. The Higgs boson was theorised in 1964, but its discovery took almost 50 years. Finally in 2012, it was discovered by the ATLAS and CMS experiments at the LHC, which was a great success for the Standard Model.

The boson responsible for the gravitational interaction is called graviton and is expected to have a spin of 2. It was theorised in the 1930s, but has not yet been discovered nor included in the Standard Model.

Electromagnetic force and photons

The electromagnetic force is very well known and imaginable to people in everyday life. It is carried out by photons, which are particles with zero mass, causing the range of the electromagnetic interaction to be infinite. Electromagnetism acts upon particles with non zero electric charge. It is responsible for electron binding in atomic nucleus and for chemical bonds between atoms creating molecules. The coupling constant, which defines the relative strength of the interaction, for the electromagnetic force is also known as the fine-structure constant and for low energies equals $\alpha_{\mathrm{EM}} = \frac{1}{137}$.

The weak force and its bosons

The weak interaction affects all quarks and leptons, however, it is of very limited ranges of approximately 10^{-18} m, due to the large mass of its intermediate bosons. These are the $\mathrm{W}^{\pm}$ and Z^{0} bosons. The weak interaction is rather different than the other interactions due to its violation of conservation laws, such as parity conservation or conservation of charm or strangeness. This fact comes into existence as the weak interaction can change the flavour of quarks, for example in β-decay, where a neutron may decay into a proton by changing one of its down quarks into up quark and vice versa.

The strong force and gluons

The strong force is the cause of nucleons holding together. With the relative strength of $\alpha_S \approx 1$, it not only holds nucleons as a whole, it also keeps positively charged protons and neutral neutrons together forming nuclei. The range of the interaction is in the order of 10^{-15} m (fm) and its strength rises with increasing range.

The strong force affects particles with non zero colour charge discussed earlier. The intermediate particles for the strong interaction are called gluons. They provide quarks with the ability to change their colour by exchanging gluons, which results in the impossibility of gluons being in a colour singlet state as they would not be able to change the colour of quarks. Combined with the symmetry principles resulting from the group SU(3), gluons create an octet of combinations.

Together with quarks, gluons constitute the proton structure. Unlike in real life, where the structure of things (buildings, people etc.) remains static, the proton is a mixture of arising and perishing quarks and gluons. Their constant change in their number combined with their fast movement creates a dynamic state. This structure is studied through the interaction of a projectile and a test particle in ultra-peripheral collisions, where the probe is the electromagnetic interaction. The projectile behaves as a source of photons, which may interact in several ways with the test particle.

2.2 Definition of some basic concepts

Impact parameter

The impact parameter b is the perpendicular distance between the path of the projectile and the centre of the target. In ultra-peripheral collisions (UPCs), the impact parameter is larger than the sum of the radii of the colliding particles.

Cross section

The cross section σ is one of the most important concepts in particle physics. It represents the probability of a specific process. The differential cross section, defined as $\frac{\mathrm{d}\sigma}{\mathrm{d}\Omega}$, states the probability of producing a scattered particle per solid angle. The total cross section σ_{tot} is obtained by integrating the differential cross section over the full solid angle

$$\sigma_{tot} = \oint \frac{\mathrm{d}\sigma}{\mathrm{d}\Omega}\mathrm{d}\Omega = \int_0^{2\pi}\int_0^{\pi} \frac{\mathrm{d}\sigma}{\mathrm{d}\Omega}\sin\theta\,\mathrm{d}\theta\,\mathrm{d}\varphi. \tag{2.1}$$

Although the SI unit for cross sections is m^2, particle physics usually uses smaller units called barns, where $1\,\mathrm{b} = 10^{-28}\,\mathrm{m}^2$.

Luminosity

Luminosity L is the ratio of the number of events N detected in a certain time t with the cross section of σ

$$L = \frac{1}{\sigma}\frac{\mathrm{d}N}{\mathrm{d}t}. \tag{2.2}$$

The units of luminosity, $\mathrm{cm}^{-2}\mathrm{s}^{-1}$ or $\mathrm{b}^{-1}\mathrm{s}^{-1}$, are determined by the dimensions of number of events per time per area.

The total amount of events detected over a time period of length T is described by the integrated luminosity L_{int} calculated as

$$L_{int} = \int_0^T L\mathrm{d}t. \tag{2.3}$$

Rapidity and pseudorapidity

The definition of rapidity is

$$y = \frac{1}{2}\ln\frac{E + p_l}{E - p_l}, \tag{2.4}$$

where E is the total energy of a particle and p_l is the longitudinal momentum. Even though the rapidity is not Lorentz-invariant, it is additive in Lorentz transformations along the longitudinal axis.

The pseudorapidity is defined as

$$\eta = -\ln\tan\frac{\theta}{2}, \tag{2.5}$$

where θ is the polar angle between the particle and the beam axis. The advantage of pseudorapidity with respect to rapidity is its dependence only on θ, which is measured easily in a detector.

2.3 Ultra-peripheral collisions in ALICE

2.3.1 Probing into the proton structure

Understanding of the structure of physical entities was always of great importance for mankind, since it teaches us about basic attributes and roles. Historically, many building blocks such as atoms or later nucleons were considered fundamental. From today's point of view, the proton is made up of quarks and gluons (particles nowadays considered to be fundamental), but the exact structure of hadrons is still a bit of a mystery.

Protons are comprised of three valence quarks, which determine their quantum numbers and other properties, combined with virtual gluons as well as sea quarks and anti-quarks. Gluons and quarks, collectively named partons, have different distributions in heavy nuclei compared with those in free nucleons. Their properties are dependent on their environment due to many factors such as the ability of gluons from different nucleons to interact together [12].

The properties of quark and gluon distributions depend also on the energy of the interaction. At very high energies, corresponding to low x values, the gluon distribution starts rising steeply. This behaviour can be seen on Figure 2.2. Nevertheless, the number of gluons cannot grow indefinitely. At some point, the gluon density will reach saturation, a dynamic equilibrium between recombination and annihilation of gluons. This phenomenon is predicted by perturbative quantum chromodynamics (pQCD), but was not conclusively observed yet. As the saturation is expected to set in for low x values, we need the highest energies possible, which are provided by the LHC.

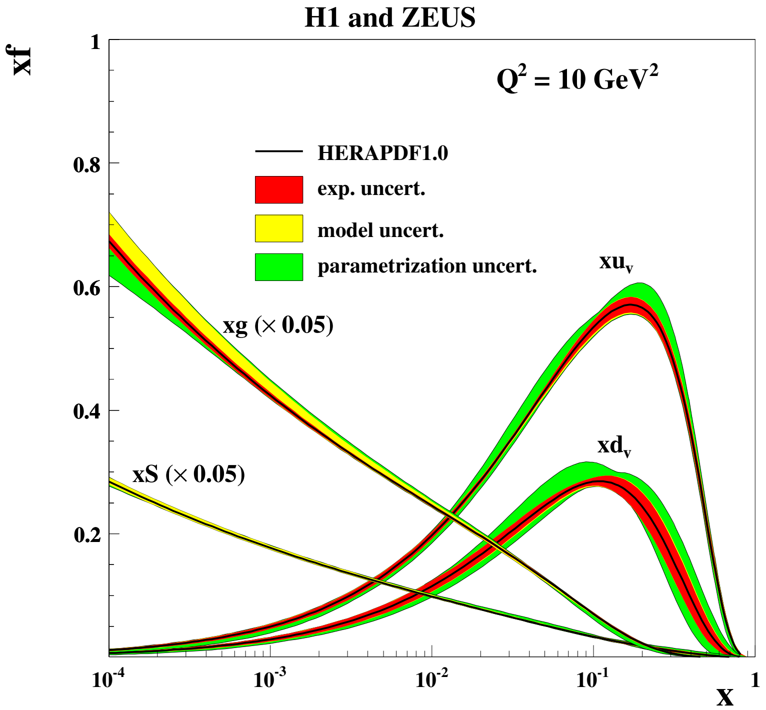

Figure 2.2: The parton distribution function at Q^2 =10 GeV^2, where xu$_v$ ∼ valence up quarks, xd$_v$ ∼ valence down quarks, xg ∼ gluons, xS ∼ sea quarks. The gluon and sea distributions are scaled down by a factor of 20 [1].

2.3.2 Vector meson photoproduction

One of the ways to study the proton structure are UPCs. These are collisions of protons and/or ions colliding with an impact parameter larger than the sum of their radii. The protons and ions, accelerated by the LHC to very high energies, can be viewed as a source of virtual photons due to their electromagnetic field. These can further interact in photon–photon and photon–hadron interactions. This provides a way to pursue collisions, where the strong force is heavily suppressed, allowing the interaction to be accomplished only by the virtual photons between the nuclei. These are also called photon-induced processes. Their cross section is very large for Pb–Pb collisions at the LHC. Expressed in numbers, the total cross section to dissociate one of the nuclei through a photonuclear process exceeds 200 barns [11].

Multiple models based on pQCD try to predict the photoproduction cross section in UPC. One of them, the colour dipole model uses that the quantum numbers of photons are the same as those of vector mesons. Thanks to this, the photon can fluctuate into a q$\bar{\text{q}}$ pair forming a colour dipole long before interacting with the target (p or Pb). The dipole then interacts with the target creating a vector meson.

Exclusive vector meson photoproduction

For the purpose of this thesis, only the exclusive VM photoproduction is discussed. That is a process, where the photon interacts with the target ion or proton creating a vector meson, a sketch of this process can be seen in Figure 2.3. During this interaction, at least two gluons interact in a way that the target and created vector meson remain colour neutral. The only particle created is a vector meson, which is further measured via its dileptonic decay. These leptons ($e^{+}+e^{-}$, $\mu^{+}+\mu^{-}$) have a clear experimental signature, e.g. the small width of charmonia makes them easy to find and measure. An event display for a J/ψ candidate produced in an ultra-peripheral Pb–Pb collision is shown in Figure 2.4.

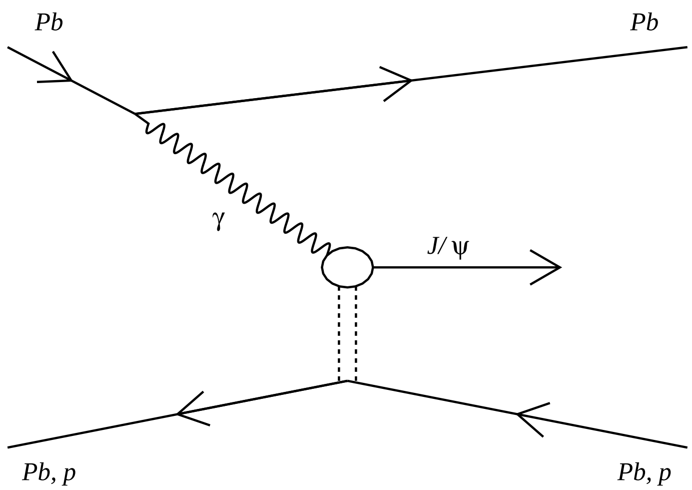

Figure 2.3: Diagram of the J/ψ photoproduction in Pb–Pb or p–Pb ultra-peripheral collision.

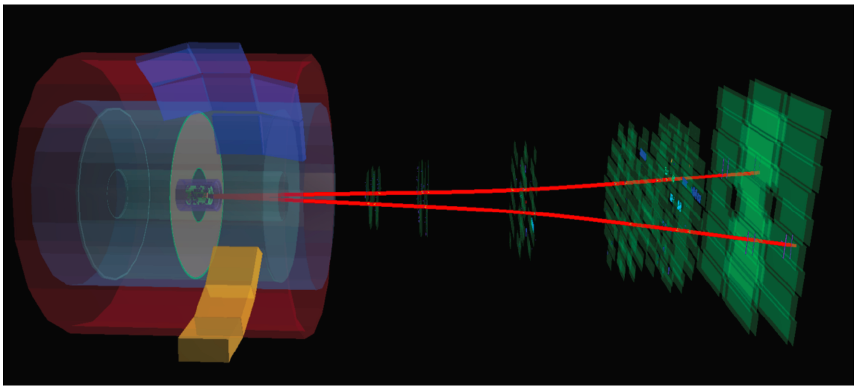

Figure 2.4: Event display for a J/ψ candidate produced in an ultra-peripheral Pb–Pb collision [11].

2.4 Use of FDD in UPC

FDD plays an important role in tagging photon-induced processes (e.g. vector meson photoproduction discussed above), which correspond to the absence of signal in the forward direction. Together with the other detectors, it helps to extend the ALICE rapidity coverage to very high values, which is fundamental for the purpose mentioned above. To achieve this it is important that the detector is fast so that signals from subsequent interactions are well separated, and that the FDD is operated at a small threshold to be sensitive even to one particle crossing it.

Chapter 3

Plastic scintillators and wavelength shifters

General information about scintillation materials is discussed at the beginning of this chapter, following with advantages and disadvantages of different types of scintillators. The emphasis is placed on plastic scintillators, because the FDD scintillator falls into this category. The wavelength shifters providing better match of emission and absorption spectra are then discussed, ending with the properties of the plastic components used in the FDD detector.

3.1 General properties of scintillation materials

Scintillators are materials showing the property of luminescence when excited by ionising radiation. Scintillation detectors in conjunction with photomultiplier tubes remain widely used in physics.

The desirable properties of a scintillation material are:

- The conversion of the particle kinetic energy into detectable light should be highly efficient.
- The light yield should be linearly dependent to the deposited energy.
- The material should evince transparency to its own emission spectrum to avoid reabsorption inside the material.
- The luminescence should have a short decay time in order to generate fast signals.
- The material should be suitable to manufacture in desired sizes at reasonable cost.
- The coupling of the light to the light sensor should be efficient.

As no scintillation material possesses all of the properties mentioned above, the choice of a particular scintillation material always depends on the intended application. The scintillators are classified into two groups: **organic** scintillators and **inorganic** scintillators. The best light output and linearity is a major feature of inorganic scintillators; however, their response time is generally relatively slow. On the other hand, organic scintillators tend to be much faster, but their yield of light is lower.

3.2 Organic scintillators

3.2.1 Scintillation mechanism

The process of luminiscence arises from transitions between the energy levels of a molecule. The organic molecules have certain symmetry properties giving rise to a π-electron structure. A sketch of the corresponding excitation levels is shown in Figure 3.1.

At room temperature, nearly all molecules occupy the S_{00} state, because average thermal energies, $kT = 0.025$ eV, are much lower than the spacing between vibrational states, which is about 0.15 eV. These molecules can be excited by an ionising radiation passing nearby to higher excited singlet states S_1, S_2, S_3 (spin 0) with energy spacing in the order of few eVs.

After the excitation, higher singlet states de-excite to the S_1 state through internal conversions, while vibrational levels states lose energy for the purpose to achieve thermal equilibrium. This process is called *vibrational relaxation*, and its duration is in the order of picoseconds (10^{-12} s). Therefore, the net effect of the excitation are molecules in the S_{10} state.

These can further emit scintillation light in three main ways. The main and desired way of emission, due to its swiftness, is prompt fluorescence, which is created by de-excitation from the S_{10} state to one of the vibrational states of the ground state S_0. The intesity of prompt fluorescence at a time t is

$$I = I_0 e^{-t/\tau}, \tag{3.1}$$

where τ is the fluorescence decay time, which is for most organic scintillators in the order of nanoseconds.

The singlet states can also be converted through inter-system crossing into triplet states, which have much larger decay times. The de-excitation from T_1 state to the ground state S_0 is called phosphorescence and its transition time can be as long as milliseconds. Since the state T_1 lies below the state S_1, the phosphorescence spectrum has a longer wavelength. Due to subsequent thermal excitation, some of the molecules may return to the state S_1 creating delayed fluorescence, which has the same spectrum as fluorescence, but the decay time is much longer.

The optical absorption and emission spectra for a typical organic scintillator can be seen on Figure 3.2. The reason, that the overlap of these spectra is rather small,

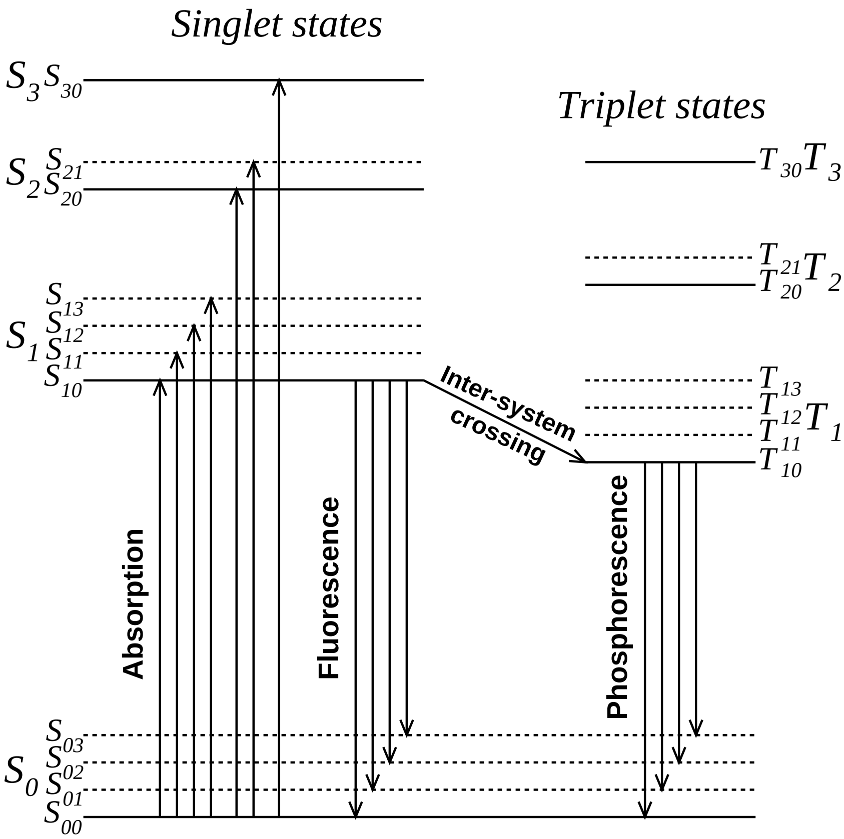

Figure 3.1: Energy levels of the π-electrons in an organic molecule, where S_0 represents the ground states; S_1, S_2, S_3 are the excited singlet states and T_1, T_2, T_3 are the excited triplet states. S_{ij} and T_{ij} are vibrational sub-levels in the corresponding states. Reconstructed according to [13].

is the fact that the photons created by the de-excitation do not have (with the exception of $S_{10} \rightarrow S_{00}$) enough energy to provide the excitation to the state S_1 or higher. This is often called the Stokes shift.

3.2.2 Types of organic scintillators

There are many types of organic scintillators such as pure organic crystals, liquid organic solutions, thin film scintillators, plastic scintillators etc. Among pure organic crystals, only two materials are widely used: anthracene and stilbene. On the one hand they may have high scintillation efficiency, but on the other hand they are

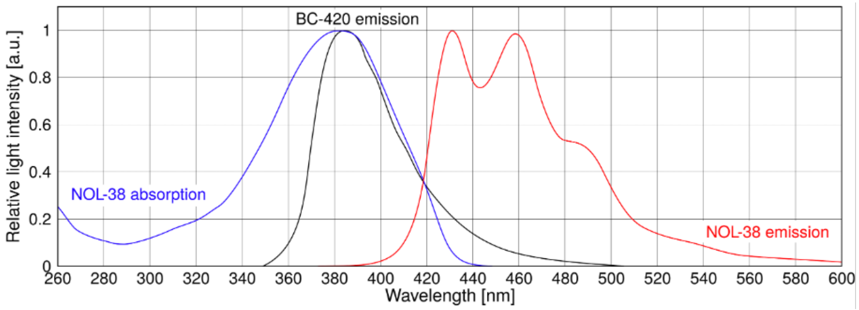

Figure 3.2: The emission spectrum for the BC-420 scintillator with the addition of the absorption and emission spectra of the NOL-38 wavelength shifter [19].

limited by their fragility and small size. The liquid organic scintillators are created by dissolution of an organic scintillator in a solvent. The benefit of liquid scintillators is the possibility of producing large volumes and their resistance to radiation damage. Thin film scintillators are very useful due to their size, as their thickness can be as low as 10 µm. They can be connected directly to the photomultiplier tube, making then very useful in fast timing measurements.

3.2.3 Plastic scintillators

One of the most useful scintillators in general are plastic scintillators. They are produced by dissolution of an organic scintillator and its subsequent polymerisation. Some of the examples are styrene, polyvinyltoluene or polymethylmethacrylate. Their biggest advantage is the possibility to produce them in various shapes and sizes with relatively small cost, but the self attenuation properties may start to play a significant role. The plastic scintillators are also available as fibres with small diameters for the purpose of measuring interactions where a good spatial resolution is needed. One the problems of plastics is their radiation resistance. Since these materials are used in places with high radiation exposure, they may show signs of degradation in the form of decreased light output or decrease in the light transmission, nonetheless it was discovered that the materials have tendencies to recover over a certain time period, a phenomenon called annealing.

3.3 Inorganic scintillators

3.3.1 Scintillation mechanism

The scintillation mechanism for inorganic scintillators is different than the one for organic scintillators. The mechanism depends on the energy states determined by the crystal lattice of the material. The electrons of the material have only discrete energy levels available, which make up the valence band or the conduction band. The electrons in the valence band are those bound at lattice sites, while the conduction band represents those whose energy is high enough to freely move throughout the crystal. The area between the valence and conduction band is called the forbidden band, since it is free of electrons. If the crystal absorbs an energy from ionising radiation, the electrons from the valence band are excited to the conduction band leaving a hole in the valence band. Their subsequent de-excitation to the valence band via photon emission is an inefficient process and in addition, the emitted photon would not have energy to lie in the visible range. Thus to increase the probability of the photon emission in the visible range, small amounts of impurities, called activators, are added to inorganic crystals The energy band structure in an inorganic scintillator enhanced with an activator is shown in Figure 3.3. The typical decay times are in the order of tens or hundreds of nanoseconds.

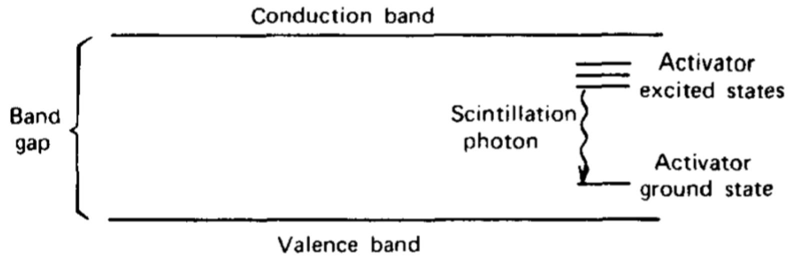

Figure 3.3: Energy band structure in an inorganic scintillator enhanced with an activator [13].

NaI(Tl)

Among inorganic scintillators, there is a superior material, sodium iodide with an added trace of thallium, which has exceptionally large light yield. This scintillator is widely used in particular in gamma-ray spectroscopy. Since its hygroscopic and deteriorates due to water absorption, it is normally preserved in an air-tight container. The dominant decay time is 230 ns, which makes it unusable for fast timing or high counting rates.

Many other interesting materials and technologies such as unactivated fast inorganic scintillators, glass scintillators or scintillator gases are also available and used.

3.4 Wavelength shifters

Wavelength shifters are used to better match the emission spectra of scintillators to the absorption spectra of photomultiplier tubes to increase their efficiency. Wavelength shifters are produced from materials which ought to absorb primary scintillation light from the scintillation molecules and reradiate it at a longer wavelength. Their important attributes are the quantum efficiency, which is the probability of wavelength-shifted photon emission per absorbed photon; and decay time, which altogether might significantly slow the light emission.

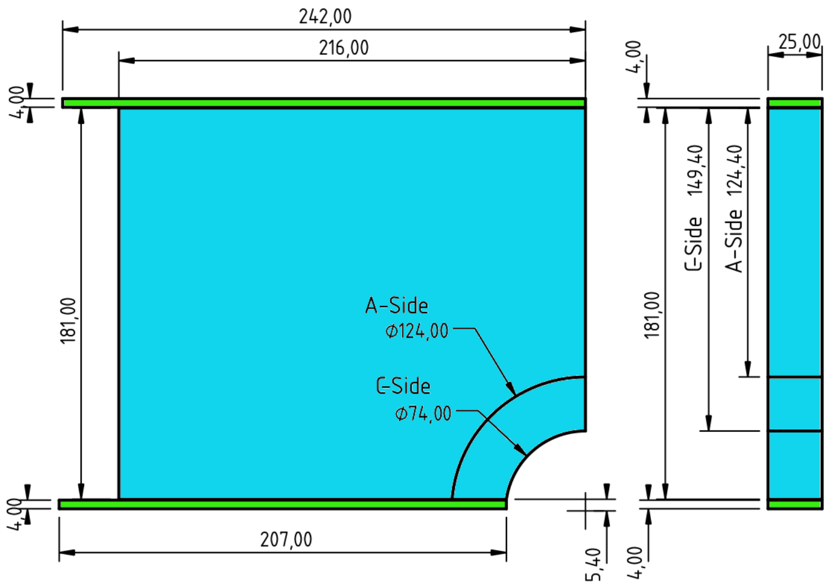

Figure 3.4: The technical drawing of FDD plastic pads. The scintillators are show in blue and the WLS bars in green. The only difference between the pads of FDD-A and FDD-C is the diameter of the inner hole as depicted by the black line [2].

3.5 The plastic scintillator of the FDD

FDD needs to be fast to avoid overlapping signals from consecutive bunch crossings. This imposes to use plastic organic scintillators for FDD, as they provide the needed speed at a reasonable cost. The technical drawing of the FDD can be seen in Figure 3.4. It consists of a scintillator module (blue coloured) combined with wavelength shifters (green coloured) at the sides to better match the absorption spectrum of the PMT. The FDD uses the BC-420 scintillator by Saint-Gobain, which is specifically dedicated to use for ultra-fast timing and counting. The BC-420 has a base of polyvinyltoluene with a refractive index of 1.58. The stated rise time is 0.5 ns, the decay time is 1.5 ns, the pulse width (FWHM) is 1.3 ns, the wavelength of max. emission is around 385 nm and the attenuation length (the distance by which the light is attenuated to $\frac{1}{e}$) is 140 cm [5]. The WLS bars used at the edges are NOL-38 by LuminnoTech, which offer a decay time of 0.95 ns [15].

Chapter 4

Photomultiplier tubes

The scintillation materials introduced in the previous chapter produce very weak light output. In order to treat the signal easily, a photomultiplier tube (PMT) converts this weak light signal into a measurable corresponding electrical signal. PMTs are able to convert a light signal as low as a single photon to millions of photoelectrons with a delay time of few tens of nanoseconds.

This chapter provides basic information about the structure of a PMT and about the technique used to convert and amplify the signal.

4.1 The principle of a photomultiplier tube

The photomultiplier tube structure

The structure of a PMT is shown in Figure 4.1. It consists of two major components: photocathode and electron multiplier, which are both enclosed in vacuum. The photocathode is a photosensitive layer, which converts the light signal into electrical signal. This is then accelerated by a set of electrodes connected to very high voltage, distributed by a voltage divider located also inside the PMT, which subsequently increases the signal to measurable values.

The photoemission process

The photoemission process begins with the absorption of the incident photon, which transfers the energy to an electron in the photocathode. This electron has to pass through the photocathode to the other side, where it is emitted. The success rate of such produced electrons is limited due to energy considerations. The potential barrier between the photocathode material and vacuum, that the electron needs to overcome to leave the photocathode, is generally about 3 eV, however, it can be reduced to values under 2 eV [13]. This potential barrier imposes a minimum energy on the photons. As the photons emitted by typical scintillators have energies about 3 eV, which is furthermore decreased by electron–electron collisions during the

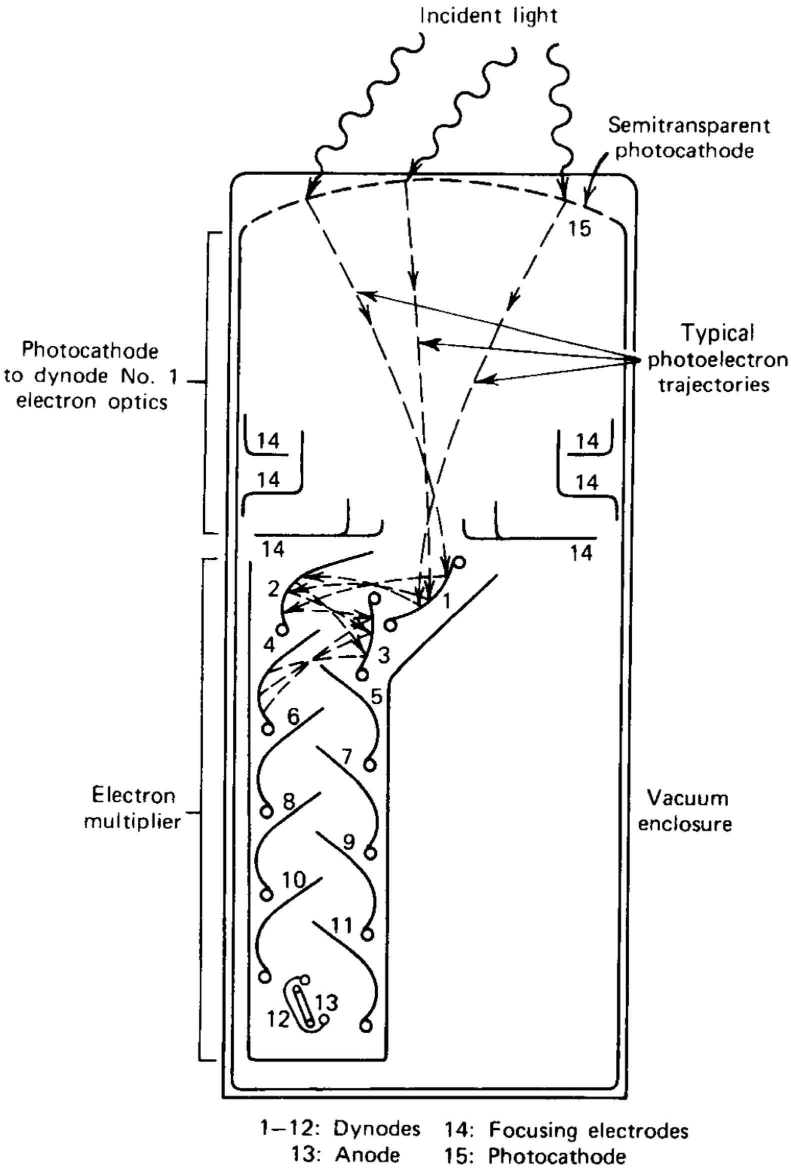

Figure 4.1: The structure of a photomultiplier tube [13].

migration of the electron through the material, the number of created photoelectrons is not nearly equal to the number of incident photons. This number is also reduced due to the photocathode thickness, which has to be as low as possible in order to avoid energy loss, but at the same time thick enough to provide the possibility for the light to interact and kick out the electrons. One of the properties of the photocathode often used is the quantum efficiency (QE), which is defined as

$$\mathrm{QE} = \frac{\text{number of emitted photoelectrons}}{\text{number of incident photons}}. \tag{4.1}$$

Due to the limitations discussed above, the standard quantum efficiencies for photocathodes are around 20-30%, however, the QE is strongly dependant on the wavelength of the incident light.

Electron multiplication

In order to make the electrical signal measurable, the primary photoelectrons from the photocathode have to be multiplied. They are accelerated by a potential difference to a set of dynodes, where they re-emit multiple secondary electrons. This multiplication created by a single dynode is given by

$$\delta = \frac{\text{number of secondary electrons emitted}}{\text{primary incident electron}}. \tag{4.2}$$

Multiple dynodes are used to achieve gains on the order of 10^6. The overall gain is given by

$$\text{overall gain} = \alpha\delta^N, \tag{4.3}$$

where α represents the fraction of all photoelectrons collected by the multiplier structure. The overall gain is a function of the applied voltage V.

4.2 Characteristics of photomultiplier tubes

The photomultiplier tubes are divided into many groups by different criteria. One of them is a division basen on their dynode structure. Some of the most common types of dynode structure are shown in Figure 4.2. The venetian blind type structure is

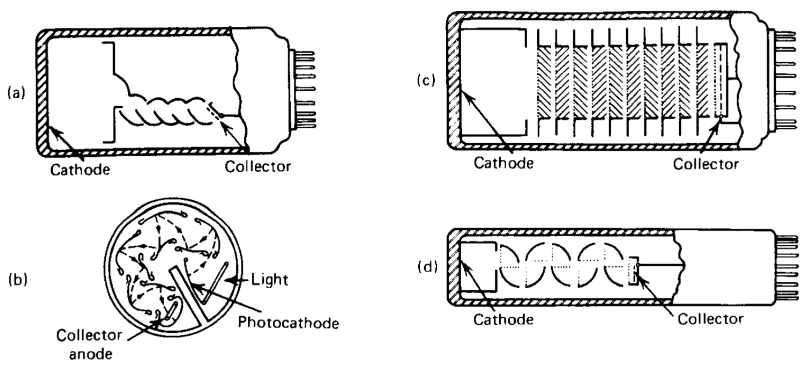

Figure 4.2: The dynode structures for common types of photomultiplier tubes: a) focused-linear type, b) circular grid type, c) venetian blind and d) box-and-grid type [13].

one of the oldest types of PMTs and have been already overcome due to their slow response time by the newer dynode structures. The box-and-grid type PMTs are slow as well, however, they are still used in tubes with large diameter. The focused-linear type and circular grid type structures were introduced to reduce the electron transit type and are used in PMTs with the fastest response time.

Nevertheless, none of the above-mentioned types is suitable for high magnetic fields, which are present at the LHC. This demand is accomplished by the fine mesh photomultiplier tubes, which are presented in the next paragraph.

Fine mesh photomultiplier tubes

The structure for the fine mesh PMTs as well as the fine mesh dynode structure is shown in Figure 4.3. This dynode structure uses mesh electrodes close together. It is excellent in output linearity and it has high immunity to magnetic fields, for which it was primarily developed [10].

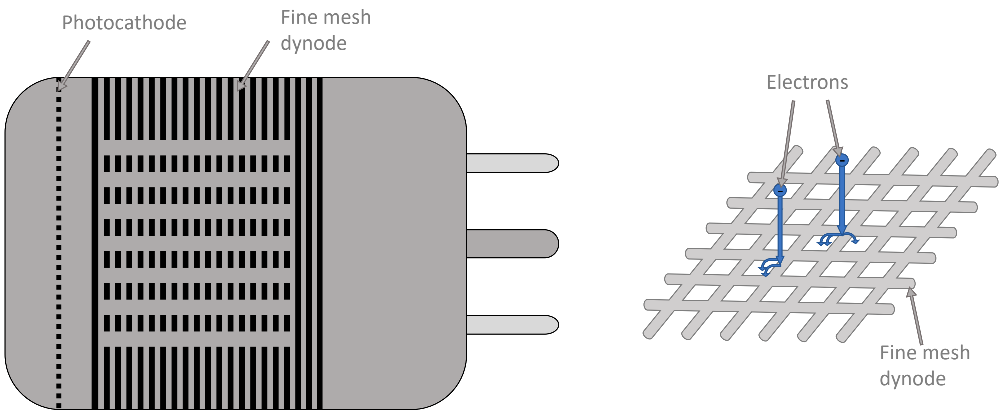

Figure 4.3: Diagram of the fine mesh photomultiplier tubes (left) and the detail of their dynode structure (right).

4.3 The FDD photosensor

FDD uses Hamamatsu H8409-70 photomultiplier tube assembly with a built-in PMT R7761-70, which is shown in Figure 4.5. The PMT has a fine mesh dynode structure (with 19 dynode stages) designed specifically for high magnetic fields (on the order of units of tesla) and its gain is 1×10^7. The photocathode is round with a diameter of 27 mm and made of bialkali. The absorbance spectrum ranges from 300 nm to 650 nm with a peak at 420 nm [16]. The plot of the quantum efficiency with respect to the wavelength is shown in Figure 4.4.

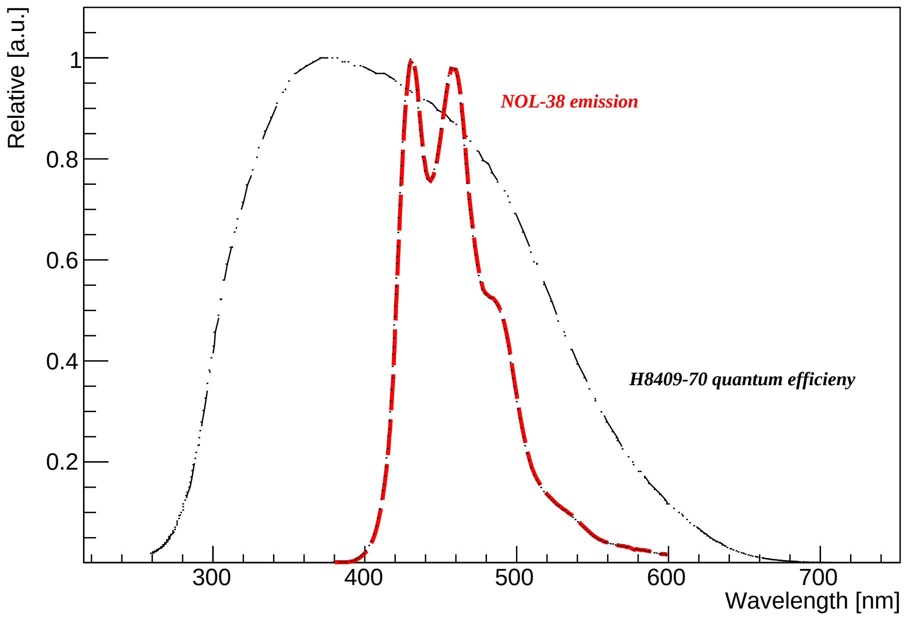

Figure 4.4: Plot of the quantum efficiency of the Hamamatsu H8409-70 photomultiplier tube assembly (black dashed line) [17] and the emission spectrum of the NOL-38 WLS bar (red dashed line).

Figure 4.5: Photo of the Hamamatsu H8409-70 photomultiplier tube assembly with the display of the high voltage (HV) and signal cable.

Chapter 5

Construction and installation of the FDD modules

This chapter provides detailed instructions for the construction of the FDD detector and its further installation. It covers the following steps of the process: the assembly and wrapping of the scintillation pads, the making of the fibre bundles, the transportation to CERN and the installation of FDD.

In total there were 20 scintillator pads prepared: 8 for FDD-A, 8 for FDD-C and two spares each for each side. There were also 20 fibre bundles prepared: 10 of length of 3 m (8 for FDD-C and 2 spares), 5 of length of 1 m (4 for FDD-A and one spare) and 5 of length of 57 cm (4 for FDD-A and one spare). The difference in length occurs due to the detector layout: FDD-C is located in the LHC tunnel and it needs long fibres to transport the light to the ALICE cavern, where the PMTs are located. Similarly, the two PMT boxes for the A-side are located at different distances from the detector, hence the reason for the two lengths.

5.1 Testing the procedure

Before starting the construction of FDD, spare parts of the predecessor of FDD (AD) were used to test the construction procedure. This test also provided the opportunity to find out the best conditions possible (working space, number of people, order of the activities etc.), improve the techniques and above all train the construction team. The testing was performed at CERN, where the construction team spent several days. Some of the construction steps with the prototype are shown in Figure 5.1.

After testing of the process with the prototypes, the construction team moved to the laboratory of the Department of Physics at the Faculty of Nuclear Sciences and Physical Engineering (FNSPE) of the Czech Technical University (CTU) in Prague, where the FDD construction took place.

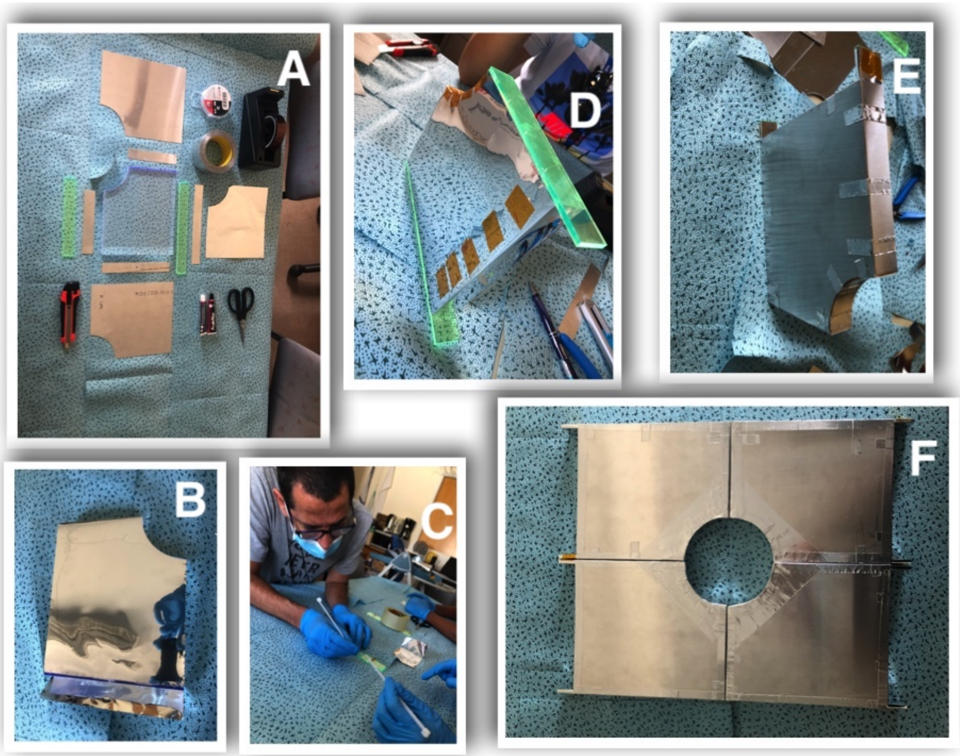

Figure 5.1: Pictures of the prototype construction: preparation of the components (A), wrapping of the scintillator (B), gluing of fishing line (C), glued wavelength-shifting bars to the scintillator (D), wrapped pad (E), four pads forming one layer of FDD (F).

5.2 Pad construction

5.2.1 Preparation for pad construction

The initial step for the preparation was cleaning and setting up the working space. A set of tables was prepared to have enough space for manipulation with the components and for laying them aside. The surface of all the tables was covered by a soft cloth (non-productive of fluff), which provided protection against scratching of the scintillator and wavelength-shifting (WLS) bars. Each of the tasks required at least two people. Nitrile gloves were used to avoid contamination of the plastic components with the oils produced by the human skin.

Once having the working space ready, all of the plastic components (scintillators and WLS bars) were washed with soap and warm water. Alcohol is never used to clean plastic scintillators, as the polyvinyltoluene, which serves as a base for the plastic scintillator, might break. The washed plastics were put aside (see pictures A and B in Figure 5.2) ready to be further dealt with.

The next step was to prepare the material used to wrap the modules as for the reflective layer. For this purpose, 3D-printed templates were manufactured thanks

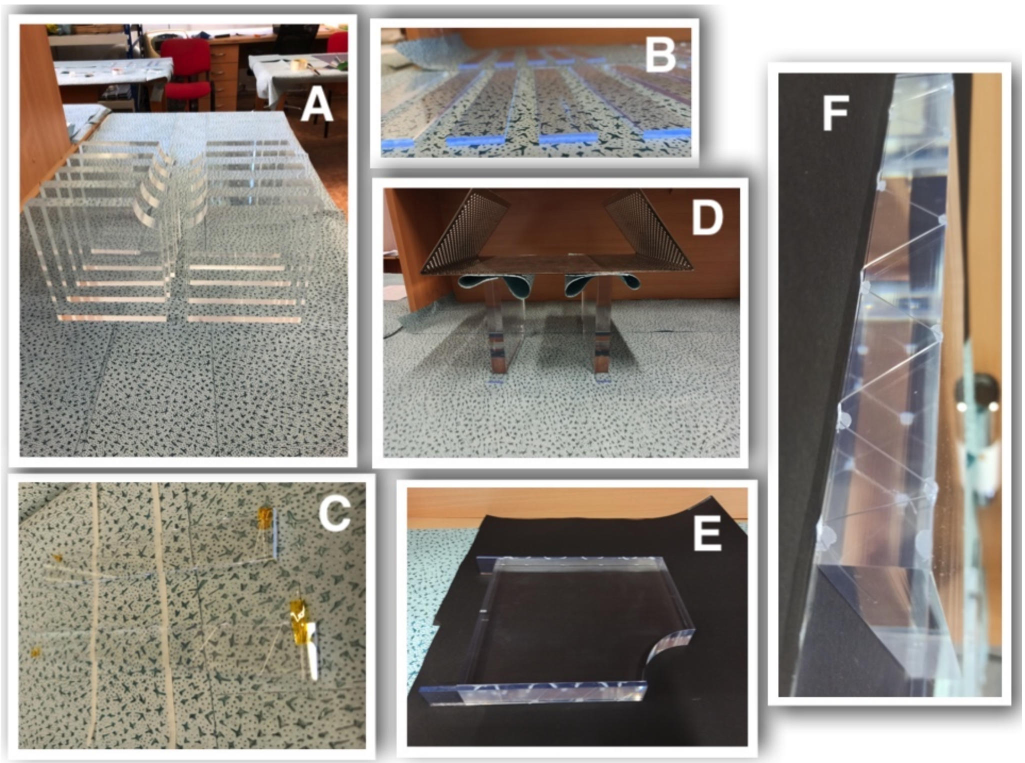

Figure 5.2: Pictures of plastic components and their gluing: plastic scintillators (A), WLS bars (B), glued fishing line to the WLS bars (C), gluing of the WLS bars to the scintillator with weight applied on top (D), plastic components glued together (E), detail of the fishing line (F).

to the help and guidance of Petr Chaloupka as shown in Figure 5.3. The printing time of the ABS parts ranged from minutes to hours for the larger pieces. These templates helped to cut the aluminium foil, which was used to wrap the scintillator (on the right side of picture A in Figure 5.4) and Mylar wrapping for the WLS bars (on the left side of picture A, pictures B, C and E in Figure 5.4). The Mylar wrapping was first cut to the exact dimensions, then pre-cut and pre-folded for easier manipulation, see pictures B, C and E of Figure 5.4. The cutting was safely done on a cutting mat covered by soft cloth as to protect both the table from scratching and the wrapping from contamination.

Aluminium plates, used as a protection for the pads, were already pre-cut to rectangular shapes. The circular cut-out in one of the corners of the biggest plates was made using a grinder. After cutting-out the rough shape, the plate was further ground with a grinder and a round file. The plates can be seen on picture D of Figure 5.4.

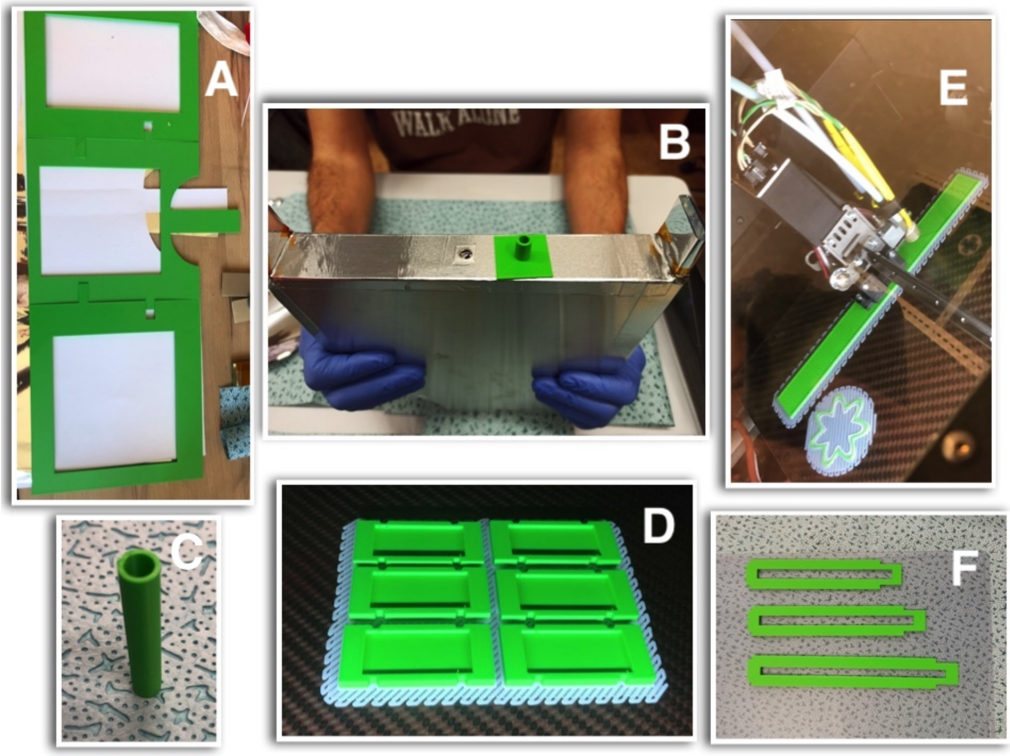

Figure 5.3: Pictures of 3D-printed ABS parts: template for aluminium foil (A), laser connector for the scintillator (B), laser connector for the PMT (C), base used for gluing of the fibre connectors (D), the 3-D printer in action (E), template for Mylar foil (F).

5.2.2 Assembly of the pads

This subsection provides instructions for the gluing of the fishing line to the WLS bars, which are then glued together with the scintillator forming a pad.

Materials needed: Wavelength-shifting bars, fishing line, Araldite glue, scissors, plastic scintillators, tool for glue mixing, disposable surface for glue mixing, tool for glue application, Capton tape, tape dispenser, cutter, weight and flush cutters.

Step-by-step procedure: The initial step is gluing of the fishing line to the WLS bars. Fishing line is used as a spacer between the scintillator and the WLS bars, because the air gap helps to trap the light inside the WLS bars.

The fishing line was attached to the WLS bar with a small piece of Capton tape approximately 1 cm from the bar edge (see picture C of Figure 5.2). The fishing line was then wound round the WLS bar to ensure its steady position, continuing with winding in a zigzag pattern (see pictures E and F of Figure 5.2). To finish the other end, 3 cm in front of the bar end, the fishing line was also wound round the bar. A piece of Capton tape was attached in order to affix the tape to the appropriate place.

Araldite glue was used to glue the fishing line to the WLS bars. It is a two component

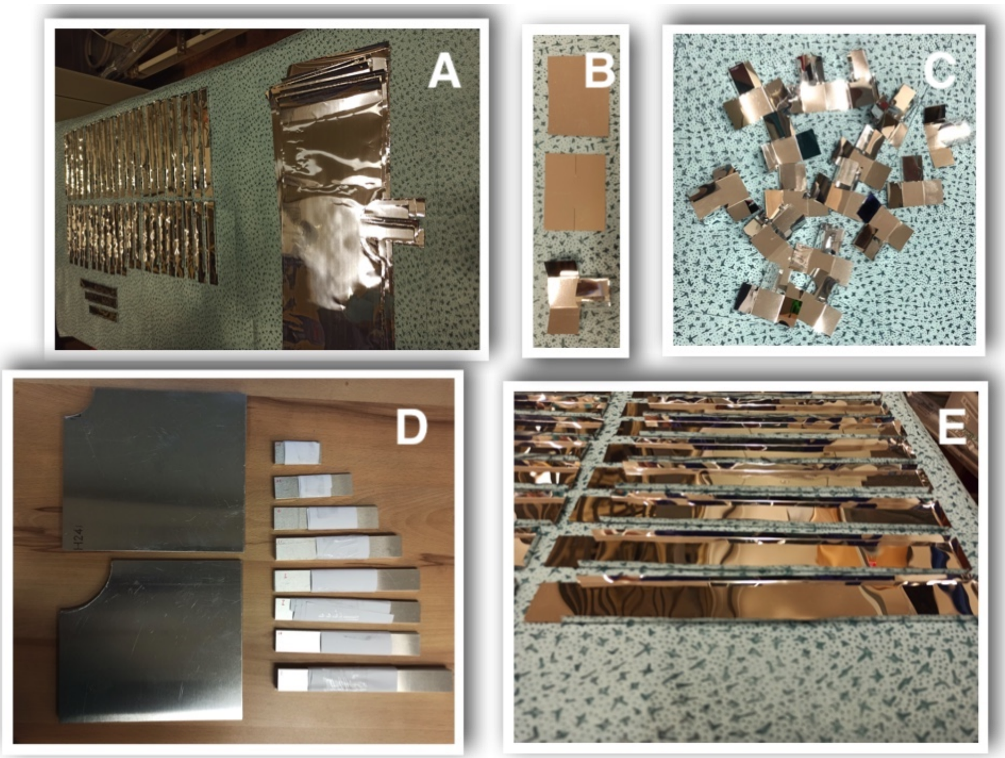

Figure 5.4: Pictures of the wrapping components: aluminium foil and Mylar wrapping (A), detail of inner Mylar wrapping (B), Mylar pieces for wrapping of the inner side of WLS bars (C), aluminium plates with the cut-out (D) Mylar pieces for wrapping of the outer side of WLS bars (E).

glue, which requires merging of the components to solidify. The components A and B of the Araldite were mixed on a disposable piece of aluminium foil with a plastic tool. A new piece of foil was used each time to ensure that the glue did not stick to any other material. The mixture was applied with a tip of a tie, because of its compactness and ease of manipulation.

A small amount of Araldite was applied to each crossing of the fishing line and WLS bar on the vertical plane (with respect to the position of the bars as shown in picture B of Figure 5.2). After gluing all of the crossings, a light weight was put on the WLS bar so as to hold the fishing line in its place. This was after let to dry out for at least one hour. When the glue was completely dry, the tape was removed and the fishing line leftovers were cut off with scissors. This procedure was repeated for all of the 40 WLS bars.

Araldite glue was also used to glue the WLS bar to the scintillator. The gluing was done in pairs (see picture D of Figure 5.2) to guarantee more stability by using a weight on the top of the pair of the pads. After mixing the Araldite as described above, it was applied to the side of the WLS bar facing the scintillator. A small amount of glue was applied, so to glue the components properly and simultaneously avoid the excess material to block the air gap. After application to one of the WLS bars, the scintillator was put on the top of the bar so they glue together and left to cure for 12 hours. The WLS bar was glued to the scintillator in such a way, that the fishing line was touching the scintillator. The procedure was repeated for all of the modules and scintillators. A complete pad is shown in the picture E of Figure 5.2.

5.2.3 Wrapping of the pads

The pad itself needs to be covered in 3 layers of wrapping. The first two layers were for reflective purposes and the last one was for protective purpose. The reflective layers should provide proper light insulation, i.e. block the incoming external light into the module. That said, this particular task was done very carefully to ensure the intended quality of the detector.

Materials needed: completed pad, aluminium foil, Mylar wrapping, Capton tape, tape dispenser, aluminium tape, aluminium plates, tool for evening out the tape, scissors and 3D-printed laser connector for the scintillator.

Step-by-step procedure: The pad was firstly covered in a previously prepared aluminium wrapping (see picture A of Figure 5.5). The foil was wound around the pad and folded on the edges using a pen with a sharp, but soft, end. The wrapping was few millimeters shorter on one side so it did not push the overlap from the edge. On the other side, the wrapping was few centimeters longer to properly seal the edge. The primal layer, after being properly aligned, was taped as shown in picture B of Figure 5.5 (the hole in the middle is later used for the insertion of a fibre, which carries the laser light from the laser calibration system into the plastic pad).

The WLS bars were covered by a Mylar foil. The pad was put on a roll of tape covered by a soft cloth with the bar ends facing the table. The Mylar wrapping (shown in picture E of Figure 5.4) was attached from top to bottom using Capton tape. The inner sides of protruding ends of the bars were wrapped using pieces shown in picture B and C of Figure 5.4. After proper alignment, they were also attached with Capton tape. The pad wrapped in the first layer is shown in picture B of Figure 5.5.

Due to unsatisfactory results of testing for light leaks of the pads wrapped in one layer of reflective covering, which will be further discussed, the second reflective cover was added to ensure better light insulation, in particular on the edges. This testing was done only for the first few fibres and the addition of the second reflective layer was automatically perform for all of the other pads. The pad was wrapped into the foil as shown in the picture C of Figure 5.5. The detail of wrapping the cut-out is shown in picture D of Figure 5.5. Further light insulation was provided by a piece covering the cut-out as shown in picture E of Figure 5.5. All of the wrapping mentioned above was fixed with Capton tape.

The protective layer is included to provide protection against damage that might happen during various manipulation and transportation processes. The protection is done with aluminium plates, which are fixed directly to the pads covered by reflective foil. The plates were simply put on the pad (see picture A of Figure 5.6) and attached together with a small piece of aluminium tape surrounding the vertical plane (see pictures B and C of Figure 5.6). A hole was drilled through the plate

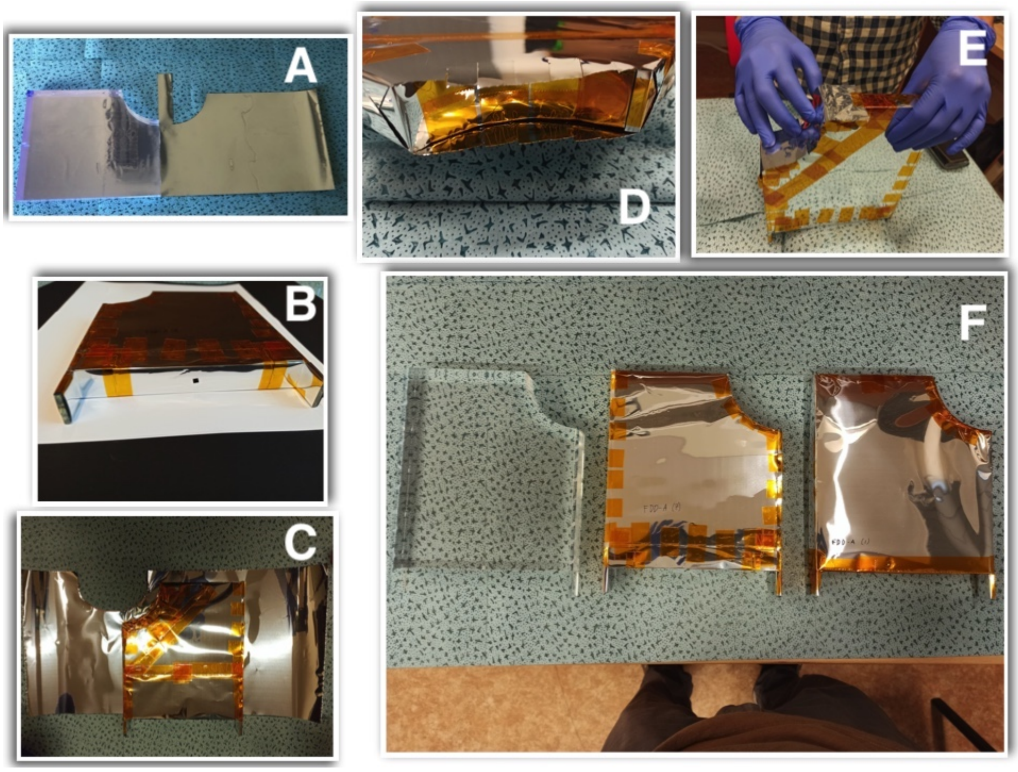

Figure 5.5: Pictures of the reflective wrapping: wrapping into the primal layer (A), taping of the primal layer (B), wrapping into the secondary layer (C), details of handling the cut-out (D) and (E), three stages of pad wrapping: naked, covered in one reflective layer, covered in two reflective layers (F).

situated between the bar endings to avoid covering of the opening for the fibre carrying the laser light. The plate covering the cut-out was hand-bent to the correct shape.

After attaching all of the plates, each of the edges was overlapped with a wider aluminium tape to provide better support and light insulation (see picture C of Figure 5.6). A 3D-printed laser connector was taped to the place of the hole as shown in the picture B of Figure 5.3. Every joint of the tape and plate was then taped again with the wider aluminium tape to provide better light insulation (see pictures D and E of Figure 5.6). Small pieces of tape were also added to the bar endings to reduce the light leaks. Finally, the pad was then finished ready to be assembled with the fibres as shown in picture E of Figure 5.6. The wrapping procedure took about one hour for a skilled pair of workers per one pad.

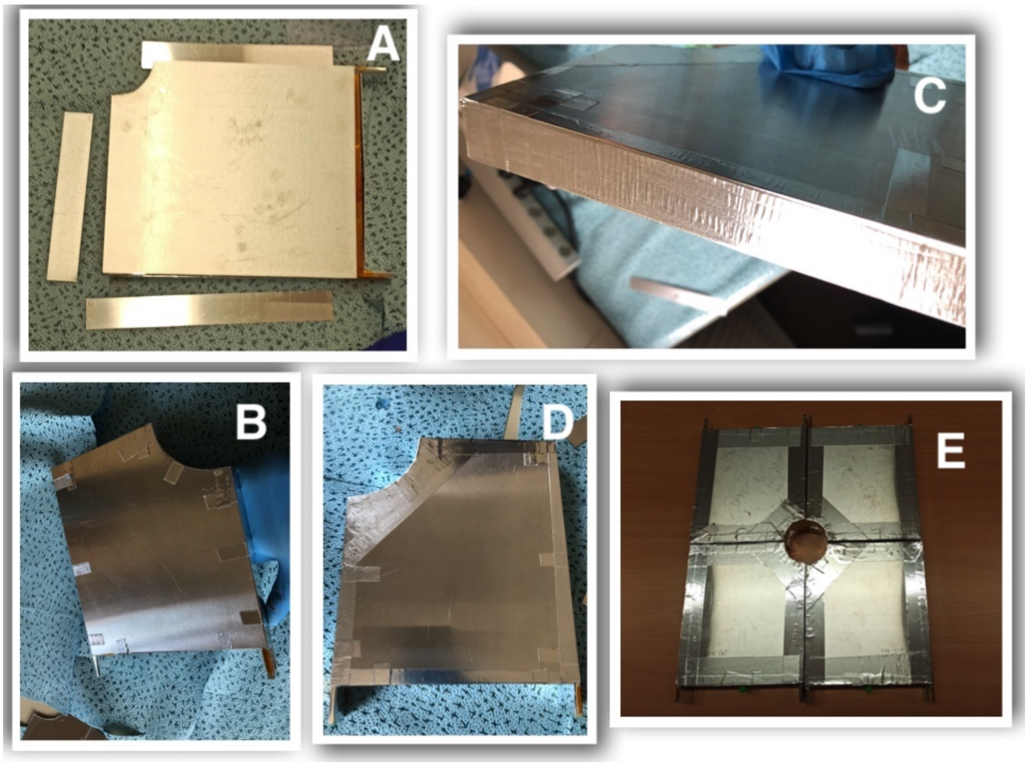

Figure 5.6: Pictures of the protective wrapping: aluminium plates in their corresponding positions (A), plates attached to one another by aluminium tape (B), detail of the edge overlapping with the wider tape (C), detail of the cut-out overlapping with the wider tape (D), finished pads forming one layer of the FDD-C detector (E).

5.3 Fibre bundle construction

5.3.1 Preparation for fibre bundle construction

As always, the first step was to clean and set up the working space (see picture A of Figure 5.7). Several tables, covered by a soft cloth, were used for the fibre bundle construction in order to have enough space for the manipulation, more so for the long fibres (see picture B of Figure 5.7). Each of the tasks required at least two people. Nitrile gloves were used as a protection against potential contamination of the components.

After setting up the working space, the first step was to unpack the fibres and separate them in individual bunches with the desired number of fibres. These fibres were obtained from the provider as 9 packages of 200 1-metre long fibres, 1 package of 120 1-metre long fibres and 9 packages of 200 3-metre long fibres with 1 package of 120 3-metre long fibres. These needed to be separated into bunches of 96 pieces of the same length. The separation of 1 package started off with the separation to bunches of 20 fibres (see picture A of Figure 5.8). Five of these bunches were then merged together and after that, four fibres of this 100-fibre bunch were put away.

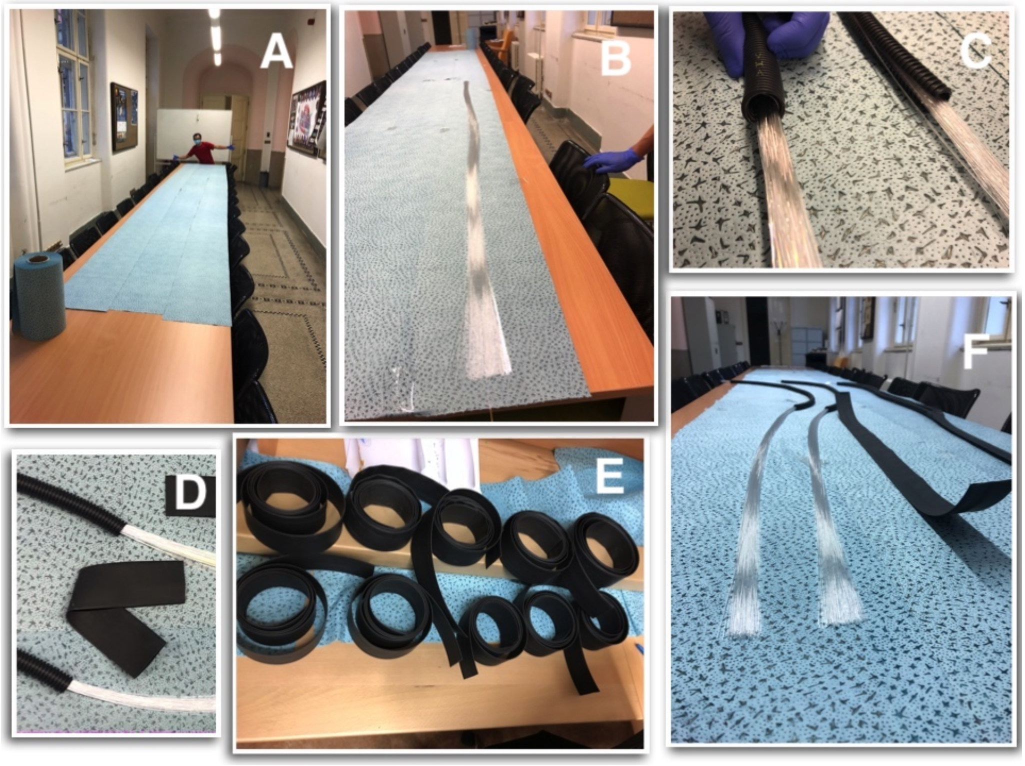

Figure 5.7: Pictures of the fibre bundle preparation: space preparation for handling the 3-metre long fibres (A), the 3-metre long fibres (B), enclosing the fibres by resealable corrugated tube (C), pre-cutting of the termofit covering (D) and (E), demonstration of the termofit position (F).

Two bunches of 96 fibres and 1 bunch of 8 fibres were obtained this way from the original package of 200 fibres. The counting was done precisely and cross-checked multiple times to ensure the right number of fibres. The separated bundles were then taped with teflon tape (used because of its inertness) on both ends (see picture D of Figure 5.8) to prevent any traversing between the bunches as they were put away (see picture C of Figure 5.8). Special care was taken that the fibres did not twist around each other; this was particularly complicated for the long fibres. Half of the 1-metre fibres was cut short to 57 cm using an office paper guillotine as shown in the picture B of Figure 5.8.

After the division, the short fibres were pushed into the termofit wrapping in order to provide protection. The long fibres were enclosed by a two-piece resealable corrugated tube as shown in the picture C of Figure 5.7. The termofit wrapping for the long fibres was also prepared (see picture D and E on Figure 5.7), but they were not wrapped until the shaping of the rectangular connectors, which will be further discussed, was finished.

The preparation continued with the supporting teflon moulds used for shaping of the connectors. The teflon pieces of the mould were cut out of two teflon slabs using a table circular saw (shown in the picture A of Figure 5.9) thanks to the help and guidance of Libor Škoda. The ABS base was 3D-printed (shown in the picture D of

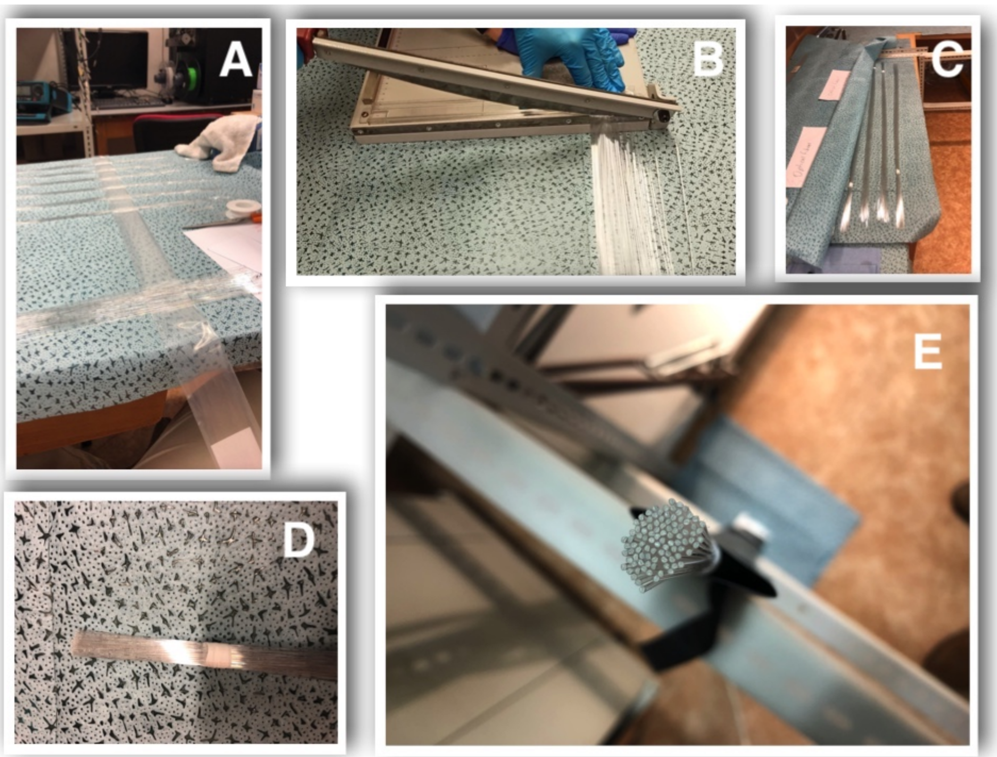

Figure 5.8: Pictures of the fibre bundle preparation: separation of the fibres (A), shortening of the fibres using an office paper guillotine (B), stowage of the separated bunches (C), detail of the detachment using teflon tape (D), detail of the fibre bunch (E).

Figure 5.9). One of the slabs was grooved before the cutting to 5 cm × 5 cm pieces (see picture B of Figure 5.9), while the other slab was just simply cut to pieces of the same dimensions. A hole in each corner was drilled into each piece (see picture C of Figure 5.9), so the two pieces of teflon could be later screwed together to form the mould (see picture D of Figure 5.9).

The PMT case with a circular teflon piece (see picture F of Figure 5.9) was manufactured in Mexico (CINVESTAV, Department of Physics), only the holes (see picture E of Figure 5.9) were drilled at our laboratory using a standing drill with various drill bits.

5.3.2 Shaping of the connectors

In order to efficiently connect the WLS bars with the fibres and the fibres with the PMT, the corresponding ends have to be of the same shape. For this purpose, the fibres were shaped into a rectangle on one side (due to the WLS bars being rectangular). Then, they were merged together to create one output for the PMT following with the shaping into a circle (due to the PMT photocathode being circular).

The teflon mould mentioned above was used so as to shape the rectangular connec-

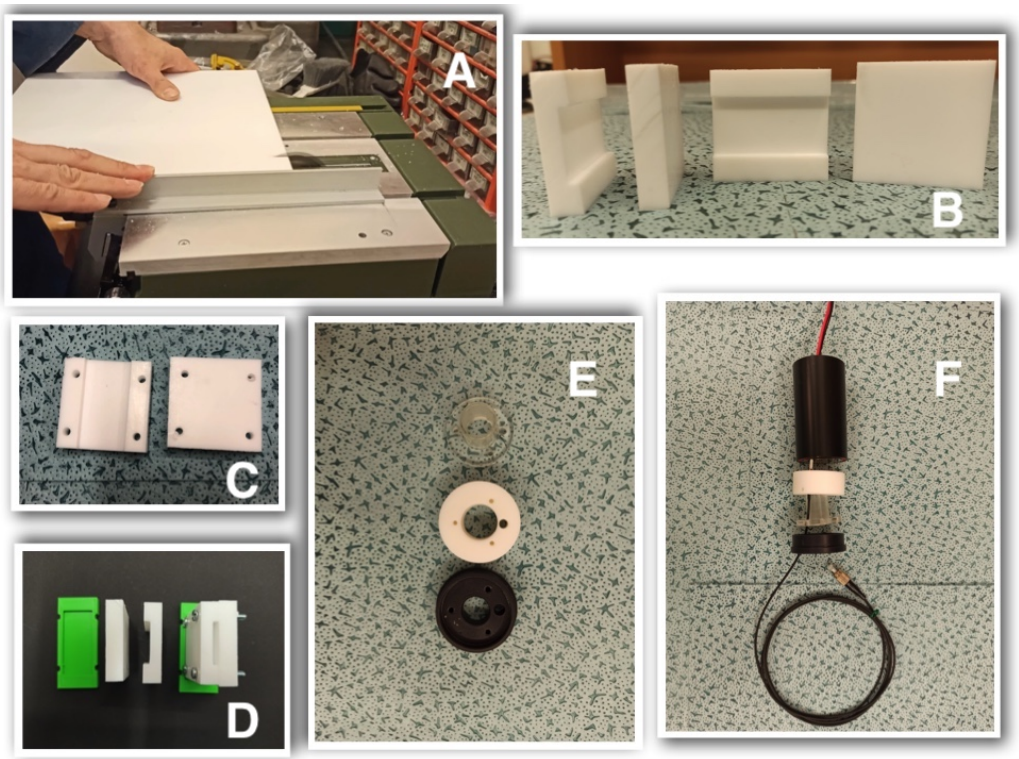

Figure 5.9: Pictures of teflon preparation: cutting of the teflon slabs to 5 cm × 5 cm pieces (A), detail of the smaller pieces (B), teflon pieces after drilling (C), assembly of the mould used for gluing (D), cap of the PMT case after drilling (E), illustration of the placement sequence inside the PMT case (F).

tors. The fibres were first slid into the teflon piece with the groove as shown in the picture A of Figure 5.10. The other teflon piece was then attached to the bottom one and the screws were tightened slightly, so the fibres inside were still loose (see picture B of Figure 5.10. To ease the polishing of the ends, the fibres were first properly aligned to the order of millimeters and only then the mould was properly tightened. A 3D-printed base with teflon tape wound around (see picture C of Figure 5.10) was used to prevent glue leaks from the mould. The base was fixed to the teflon piece bolted together using six pieces of rubber bands, three for each side (see picture F of Figure 5.10). The prepared fibres were then placed vertically and fixed to a supporting structure 10 cm from one another (see picture G of Figure 5.10).

A Polytec glue was used to glue the fibres together. The glue, originally separated in two parts, was applied by a set of syringes. One syringe was used to draw in the part A, another one was used to draw in the part B. Both of the parts were put in a small plastic cup and thoroughly mixed to ensure their proper blend. The mixture was then applied by a syringe from the top of the mould as shown in the pictures D and E of Figure 5.10. The glue was applied directly to the fibres, from where, thanks to its consistency, it flowed down to the base. This ensured that the connector was well glued from top to bottom. Several lamps were used to help the glue to dry properly (see picture G of Figure 5.10). After at least 24 hours of

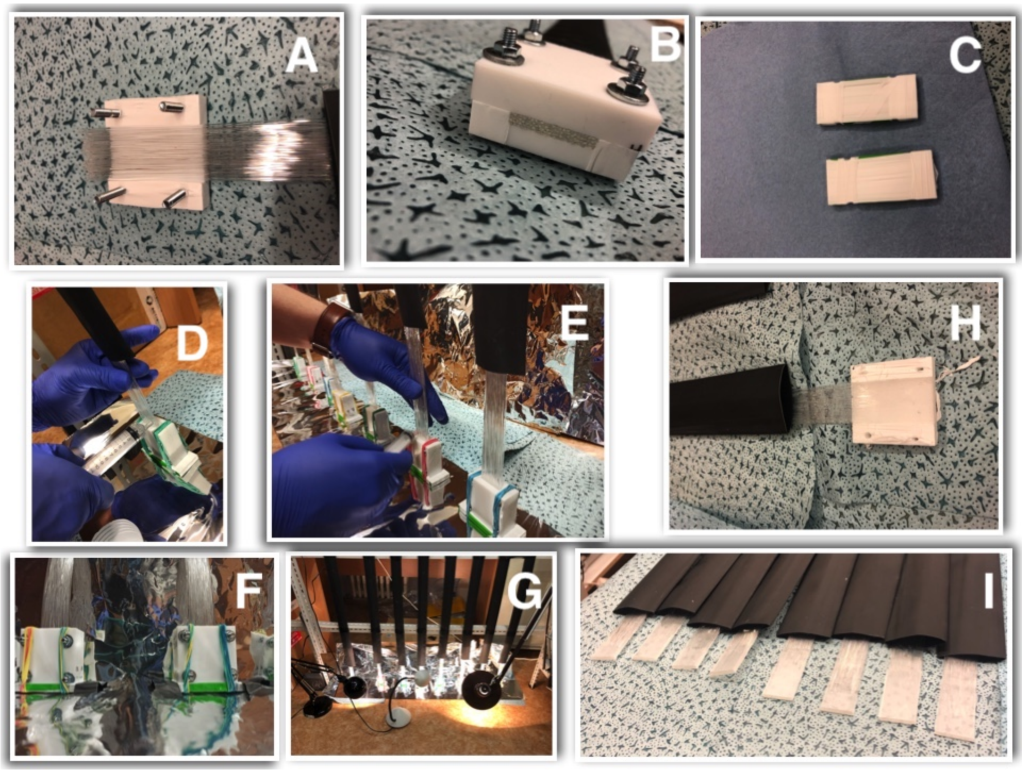

Figure 5.10: Pictures of the rectangular connectors making: bunch placed in the bottom piece of the teflon mould (A), bunch in the teflon mould (B), 3D-printed base covered with teflon tape (C), applying of the glue to the moulds (D) and (E), demonstration of the positioning during the gluing process (F) and (G), removing of the teflon mould (H), fibre bunches with shaped connector (I).

drying, the rubber bands, the base and the screws were removed (see picture H of Figure 5.10). The connector was then carefully removed from the mould to avoid damage to the fibres.

The shaping process for the circular connectors was nearly identical. The main difference was the number of fibres glued together, as the used bunch was a junction of the two bunches of 96 fibres. This is because the two fibres from both of the WLS bars combine into a single bunch connected to the PMT. The junction of the bunches is shown in pictures A and B of Figure 5.11. The shaping and gluing process can then be seen in Figure 5.11.

5.3.3 Polishing of fibre endings

The endings of the fibres were thoroughly polished to ensure the best light transmission possible. This task was done in the Faculty of Mechanical Engineering of the Czech Technical University in Prague thanks to the help of Martin Janda and František Lopot. The polishing was done by hand to provide the needed care for such delicate components.

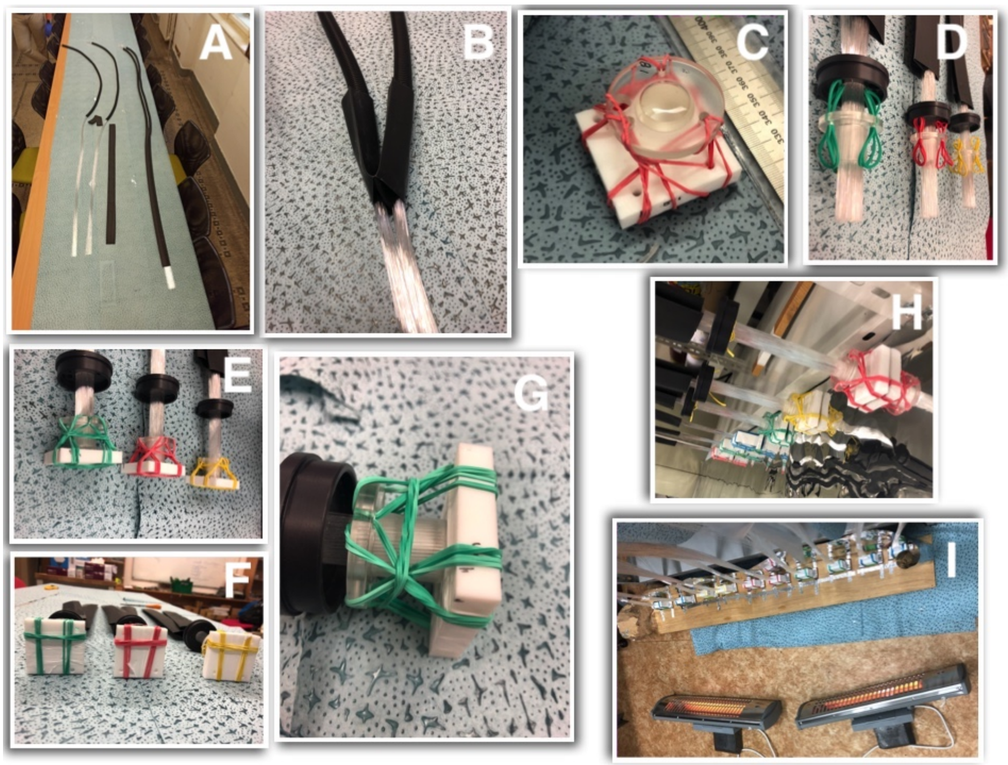

Figure 5.11: Pictures of the circular connectors making: preparation for the shaping process (A) and (B), testing of the tightness (C), preparation for attaching of the mould (D), attaching of the mould (E) and (F), detail of the securing (G), demonstration of the positioning during the gluing process (H) and (I).

The preparation of the space needed for the polishing is shown in picture A of Figure 5.12. The connector attachment is shown in picture B and C of Figure 5.12 for the rectangular and circular connectors, respectively. The securing was provided by 3D-printed parts. Picture D of Figure 5.12 shows the process of polishing. Sandpaper of various grits was used to polish the fibres as best as possible. A microscope was used to look closely at each of the endings to check the quality of the polishing (see picture E and F of Figure 5.12). The desired quality was reached when all of the individual fibres were in a plane and none of them was covered with a layer of glue.

Six out of ten long fibre bunches showed an indication of a fibre breakage. This is not optimal, but does not jeopardise the operation of the detector because the affected fibres are a very small percentage of the total number of fibres (in most cases 1 out of 192 fibres; the worst case with 5 out of 192 fibres possibly broken was used as a spare and will be repaired). None of the shorter fibre bundles (57 centimetre-long and 1-metre long) showed similar problems.

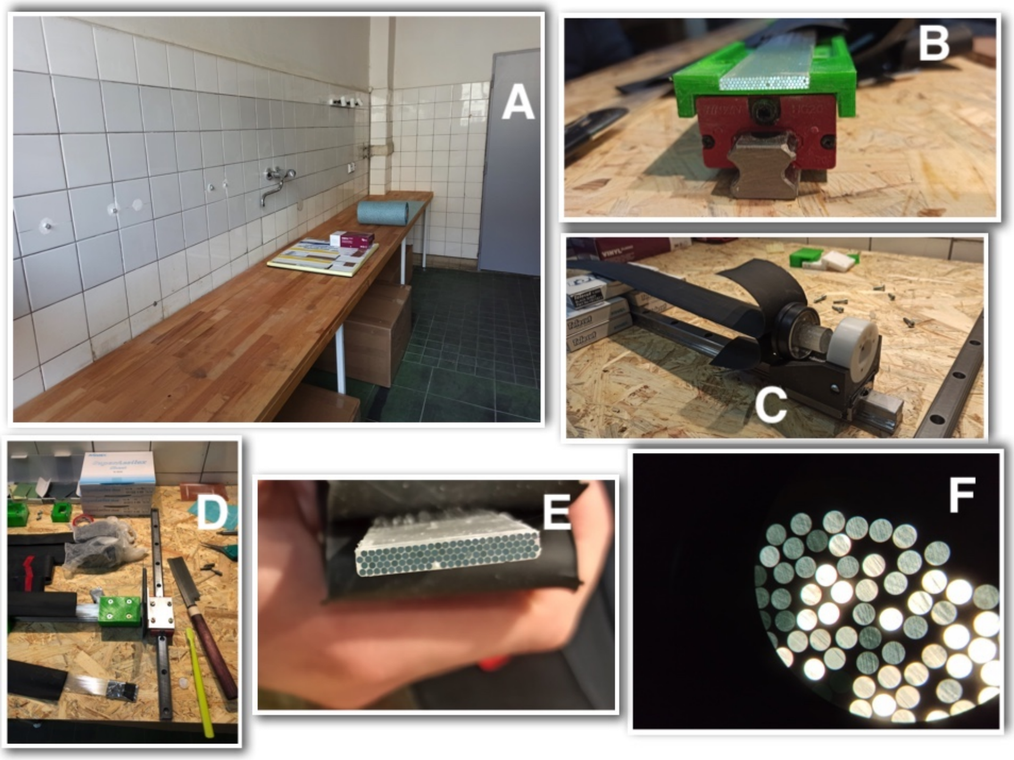

Figure 5.12: Pictures of the polishing of fibre endings: space preparation for the polishing (A), attachment of the connectors (B) and (C), polishing in process (D), polished endings: rectangular (E), circular (F).

5.4 Light-leak testing

To quantify the quality of the light insulation, the pads are connected to the PMT and illuminated by light to see how well they are manufactured (how good they keep the light out). As the pads are being tested and sealed properly during the installation, it was at this point sufficient to test them just roughly to spot any serious leak points.

To be consistent, the same piece of used AD fibres was used to transport the light, while a PMT from the AD detector, which was connected to an oscilloscope, was used as a photosensor. A phone torch was used to illuminate the pad. If the pad was not sealed properly, the illuminating light entered the pad and created a signal in the PMT, which was observed with the oscilloscope. The quality of the insulation is determined by the amplitude of the signal observed: the lower the amplitude, the better the insulation and vice versa. The setup used for the light-leak testing is shown in Figure 5.13.

Figure 5.13: Pictures of the light-leak testing: display of the setup (A), module placed in a dark box (B), detail of the covered PMT (C), insulation against outer light (D).

5.5 Packaging and transport

Since the work took place mainly in the Czech Republic, the parts then needed to be transported to CERN for their installation. As the majority of the parts are very fragile, they needed to be packed safely so they were not anyhow damaged during the transport.

The short fibres were individually covered with a bubble foil as shown in picture A of Figure 5.14. They were shipped in a cardboard box with its sides covered by LDPE foam. The box was also filled with other smaller pieces of material and tools that needed to be shipped.

Two custom cardboard boxes were made for the longer fibres, each of them storing 5 pieces. To ease the manipulation and reduce the needed dimensions, the fibres were bent into a circle. After some testing to determine how much the fibres could be safely bent, the chosen dimensions for the base of the box were 60x60 cm^2. The sides of the box were covered with 1 cm thick LDPE foam. The long fibres were stacked on each other with 1 cm thick LDPE foam between every level. The fibres were inserted into 7 cm thick LDPE foam, which covered the centre part as well as the corners (see picture B of Figure 5.14).

The box for the pads was made out of wood due to their big mass. The sides were

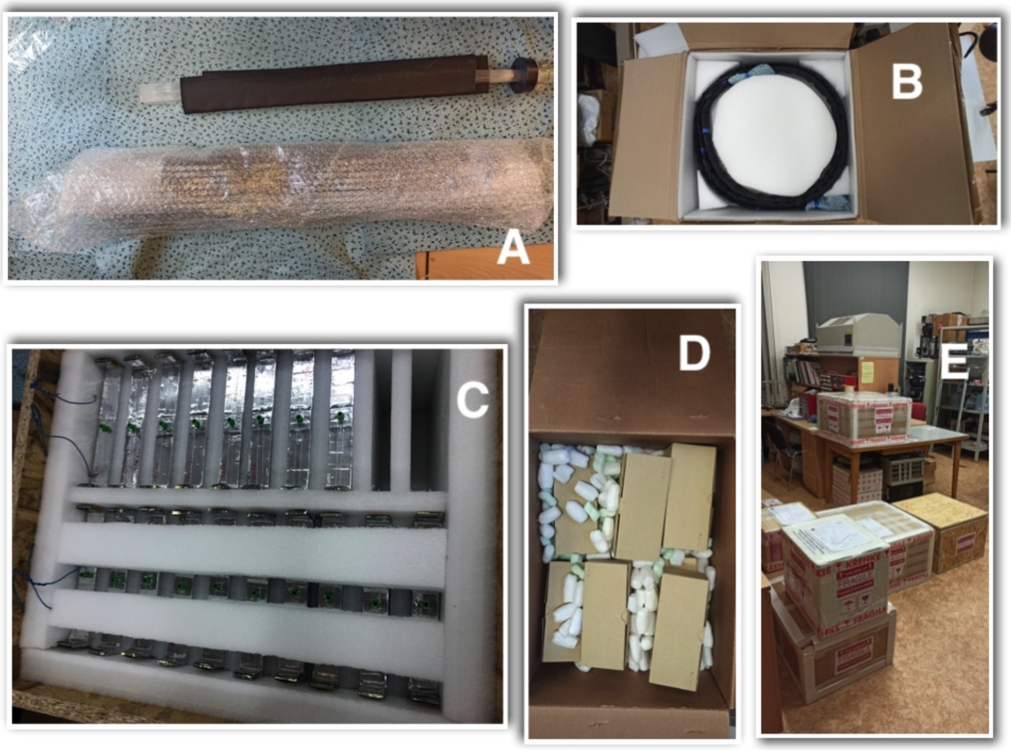

Figure 5.14: Pictures of FDD packaging: packaging of the short fibres (A), packaging of the long fibres (B), packaging of the pads (C), box with the PMTs (D), boxes ready for shipment (E).

covered with 4 cm thick LDPE foam. Two rows of the pads were placed in the box (see picture C of Figure 5.14). Two centimeter LDPE foam was wedged between indivdual pads as well as between the rows. On top of the pads, LDPE foam was also used as a protection for the WLS bar overlaps (see picture C of Figure 5.14).

Boxes with PMTs inside were stored in a bigger box filled with packing peanuts (see picture D of Figure 5.14), that protected the PMTs against vibration and shock. The inside of the PMT boxes was also covered with soft foam.

5.6 Assembly and installation

The installation of FDD is a rather complicated process. Initially, the parts have to be pre-assembled and prepared in the laboratory and only after that the installation can be realised.

In order to install the FDD, an access to the LHC tunnel and the ALICE cavern was needed. This required successful completion of numerous training courses required by CERN, namely:

- Emergency Evacuation
- Radiation Protection - Awareness
- Safety at CERN
- Electrical Safety - Awareness - Fundamentals
- Electrical Safety - Awareness - Facilities
- Self-Rescue Mask - Initial
- Radiation Protection - Supervised Area
- CERN - LHC Large Experiments
- ALICE - Surface and Underground Areas
- CERN - Beam Facilities
- LHC - Machine

5.6.1 Pre-assembly of the detector

The pre-assembly of the detector started with the installation of the optical fibres for the Laser Calibration System (LCS) to the scintillators and PMTs. The LCS is an addition that enables us to study the performance and ageing of the detector over long periods of time. It uses optical fibres connected to each of the PMTs and scintillator of the set-up. This configuration provides a way to study the properties of the laser signal coming through the optical fibres from the scintillator and compare it with the light signal applied directly to the PMT.

As for the scintillators, the optical fibres were inserted in the scintillator hole, secured with Caption tape and covered with termofit piece. A hot-air gun was used to heat up the termofit to cause its shrinking. This process is shown in Figure 5.15.

A nearly identical approach, shown in Figure 5.16, was used for the PMTs. The optical fibre was inserted into the top of the PMT case through a custom 3D-printed connector. It was pushed to the end of the connector to provide best efficiency and secured with Capton tape. Then, it was again covered with termofit wrapping. This time, a piece of cardboard was used to avoid heating of the optical fibres and their potentional harm.

After preparation of the pads and fibres, the detector was assembled. This includes only the placement of the pads into the supporting frame (same as for the AD), as the fibres are connected to the detector during the installation on site. Nevertheless, the procedure was thoroughly tested in a laboratory prior to the installation (see Figure 5.17). Additionally, the assembled detector was surveyed as it would not be possible to make proper survey after the installation due to space limitations.

5.6.2 Installation of FDD-C

The installation of FDD-C took place in the LHC tunnel and the ALICE cavern, where two teams of three people operated. It was carried out on 22 and 23 February, 2021. It started with the removal of the AD detector. The supporting frame with the detector was removed prior to the installation date, but the old optical fibres and PMTs (see picture A of Figure 5.18) had to be removed.

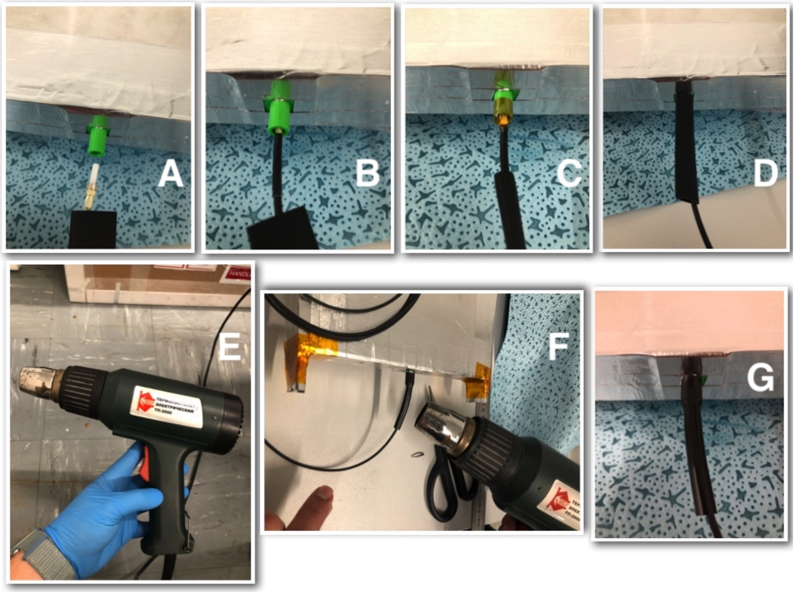

Figure 5.15: Pictures of the installation of the optical fibres for the laser calibration system for the scintillators: insertion of the laser tip to the dedicated hole (A) and (B), securing of the tip with Capton tape (C), insulation with termofit tube (D), hot-air gun (E), heating of the termofit (F), final state (G).

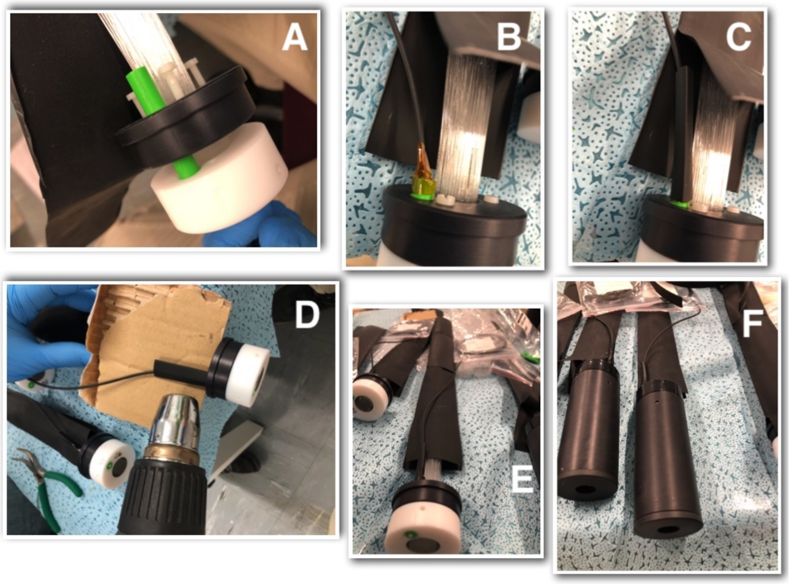

Figure 5.16: Pictures of the installation of the optical fibres for the laser calibration system for the photomultiplier tubes: illustration of the layout of the PMT-case top (A), insertion and securing of the laser tip with Capton tape (B), insulation with termofit tube (C), heating of the termofit (D), finished optical fibre: without PMT case (E), with PMT case (F).

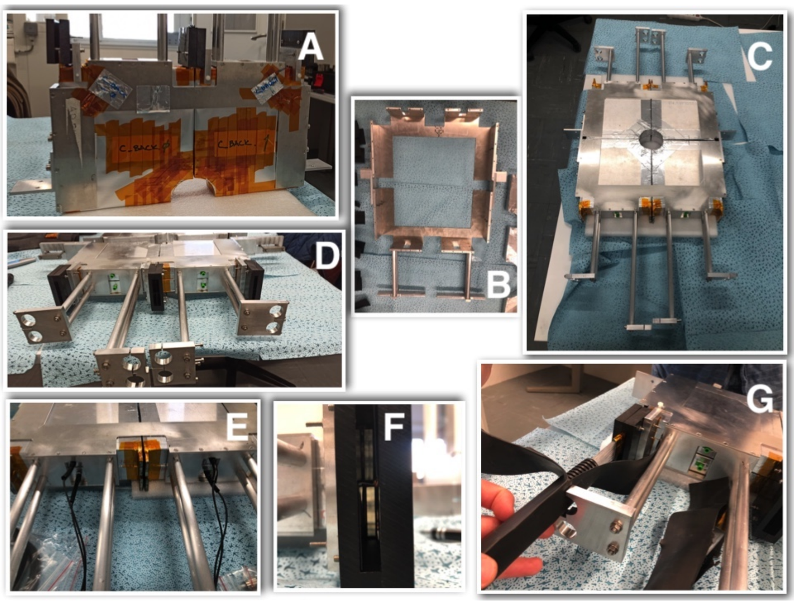

Figure 5.17: Pictures of the FDD-C assembly: FDD predecessor (AD) before uninstallation (A), aluminium supporting frame for the detector (B), illustration of the detector layout (C), supporting frame for the optical fibres (D), installed finished scintillator modules (E), detail of the frame for WLS bars (F), fibre bundle inserted into the frame (G).

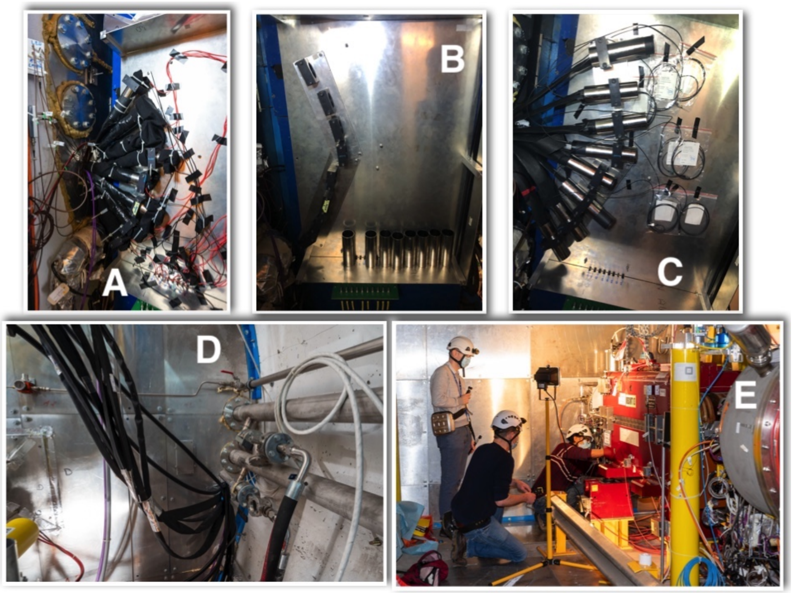

Figure 5.18: Pictures of the FDD-C installation: PMT box before the installation (A), empty PMT box (B), PMT box after the installation (C), optical fibres passing through a hole from the LHC tunnel to ALICE cavern (D), installation of FDD-C (E).

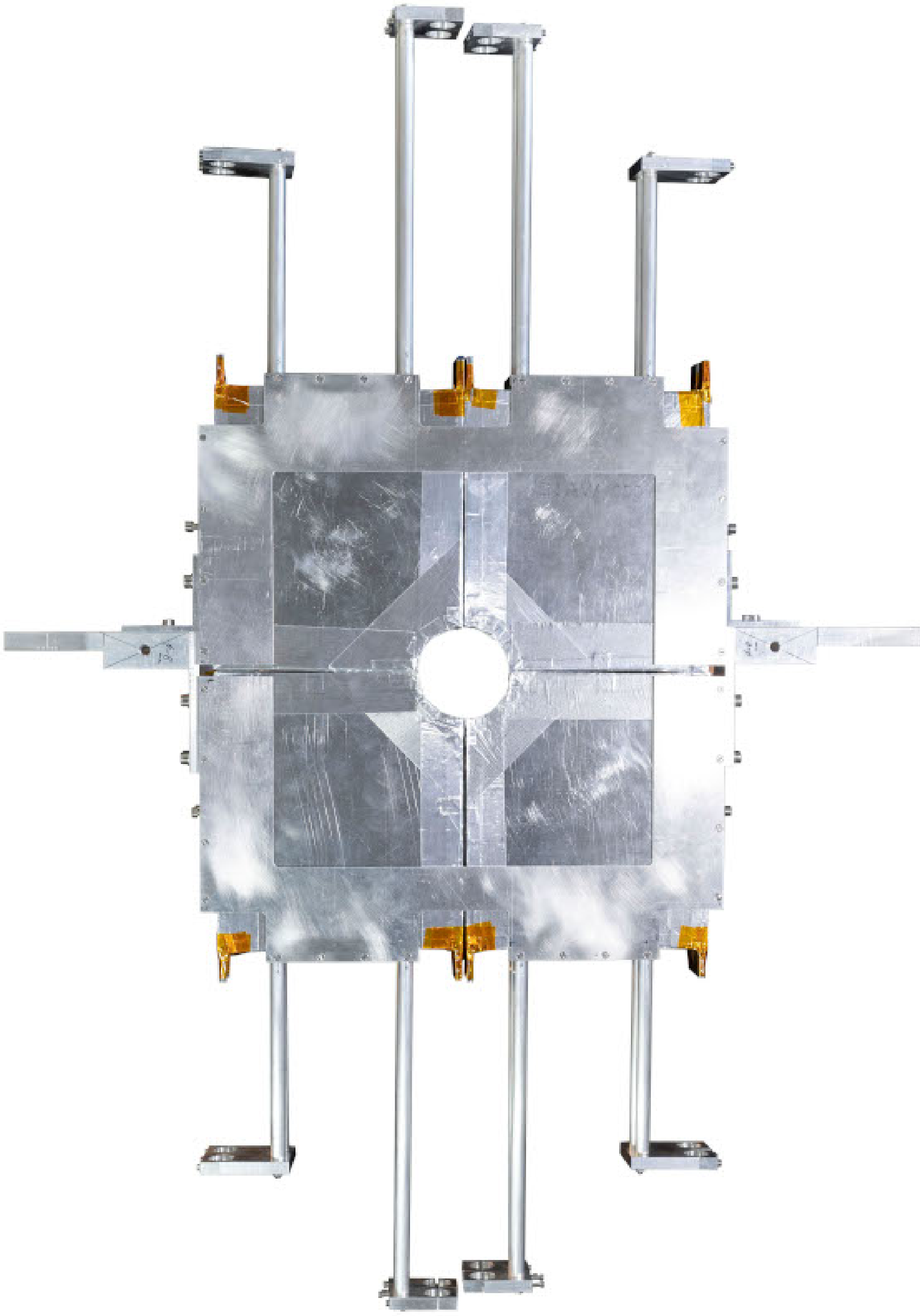

Figure 5.19: Photograph of FDD-C before installation. Courtesy of W. H. Trzaska.

After this preparation, the installation itself was executed. At first, the pre-assembly (shown in Figure 5.19) was fixed to a structure used previously for AD. The optical fibres were pushed from the cavern into the tunnel, where the tunnel team attached them to the structure and connected them to the pads. Simultaneously, the PMT cases on the fibre endings were put in Mu-metal tubes (used as a protection for the

PMTs against magnetic field) by the cavern team and fixed to the holders in the PMT box (see picture C of Figure 5.18), which is located in the ALICE cavern.

The next stage of the installation was the insulation against outer light for the PMT cases in the ALICE cavern as well as for the pre-assembly in the LHC tunnel. The insulation was done with aluminium tape. To guarantee good light insulation of the pad, an oscilloscope connected to the corresponding PMT was used for the measurement of the amplitude of the light signal produced by a phone torch illuminating the pad. Thanks to this, the spots with poor light insulation were additionally covered until the signal was independent of the illumination by the torch. A set of pictures capturing this process is shown in Figure 5.20.

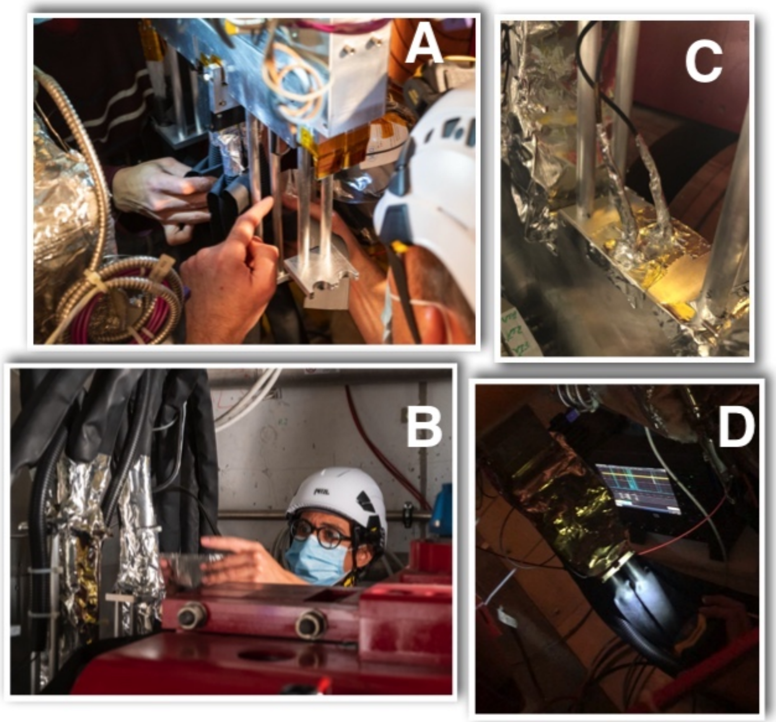

Figure 5.20: Pictures of the FDD-C installation: attaching of the fibres to the pads (A), light-leak insulation of the optical fibres (B), detail of the light-leak insulation of the LCS (C), testing for light-leaks with oscilloscope (D).

A photograph of the installed FDD-C is shown in Figure 5.21.

5.6.3 Installation of FDD-A

The installation of the A side will take place in July 2021. As for the preparation works, the scintillator pads and PMTs have the optical fibres for the LCS included, ready to be assembled into the supporting frame and installed. The PMT boxes, located near the detector, provide a safe place for the storage of the photomuliplier tubes during the detector operation. Unlike for FDD-C, which had the PMT box

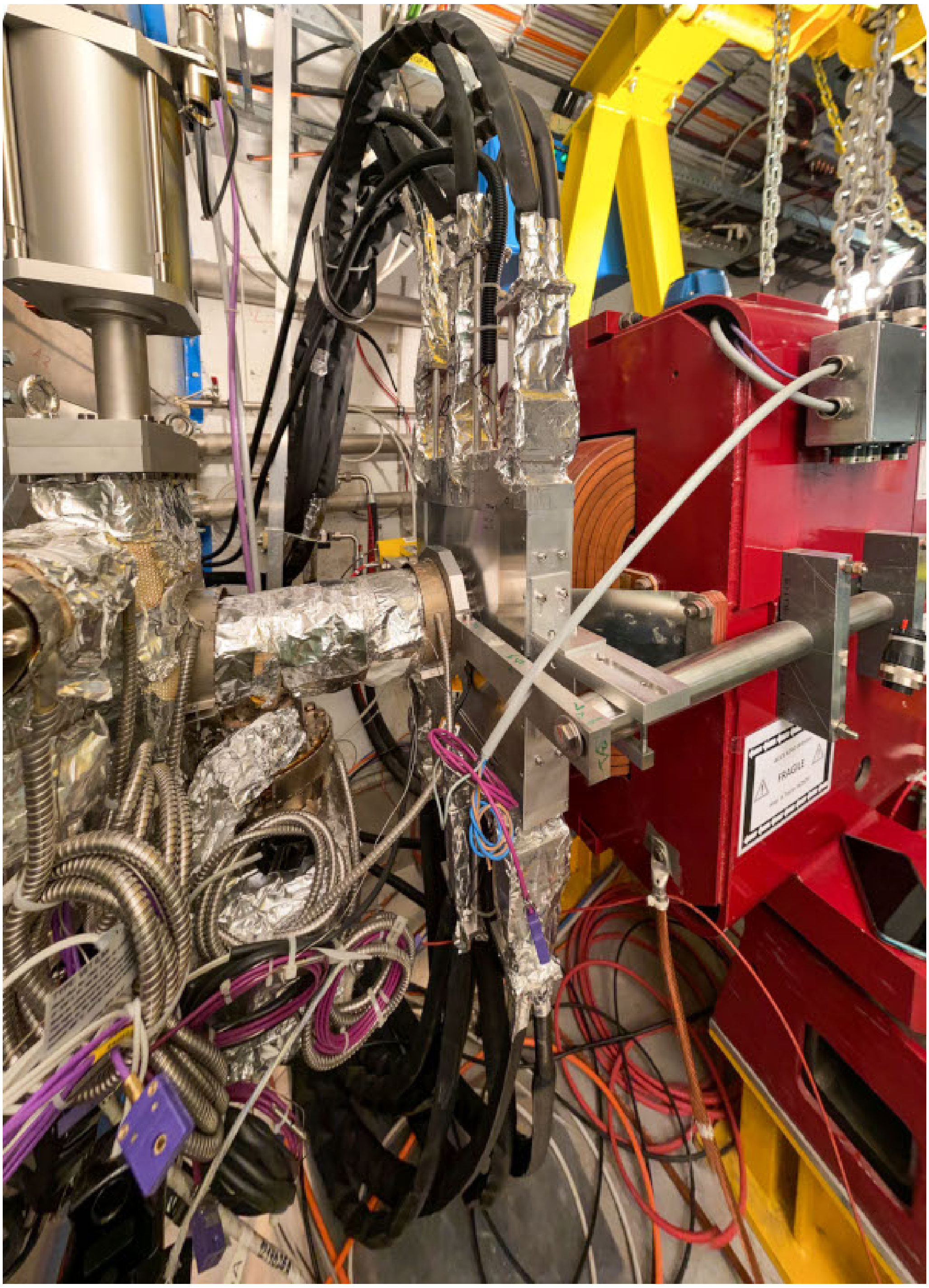

Figure 5.21: Photograph of the installed FDD-C in the LHC tunnel. Courtesy of W. H. Trzaska.

ready, the FDD-A PMT boxes (two in total, located above and below the detector, respectively) were missing and a new set had to be made.

For this purpose, a survey was done on site to acquire the dimensions of the boxes and their attachment. The boxes were made of aluminium plates (see picture A of Figure 5.22). The inside of the boxes was coated with dark paint (see pictures C

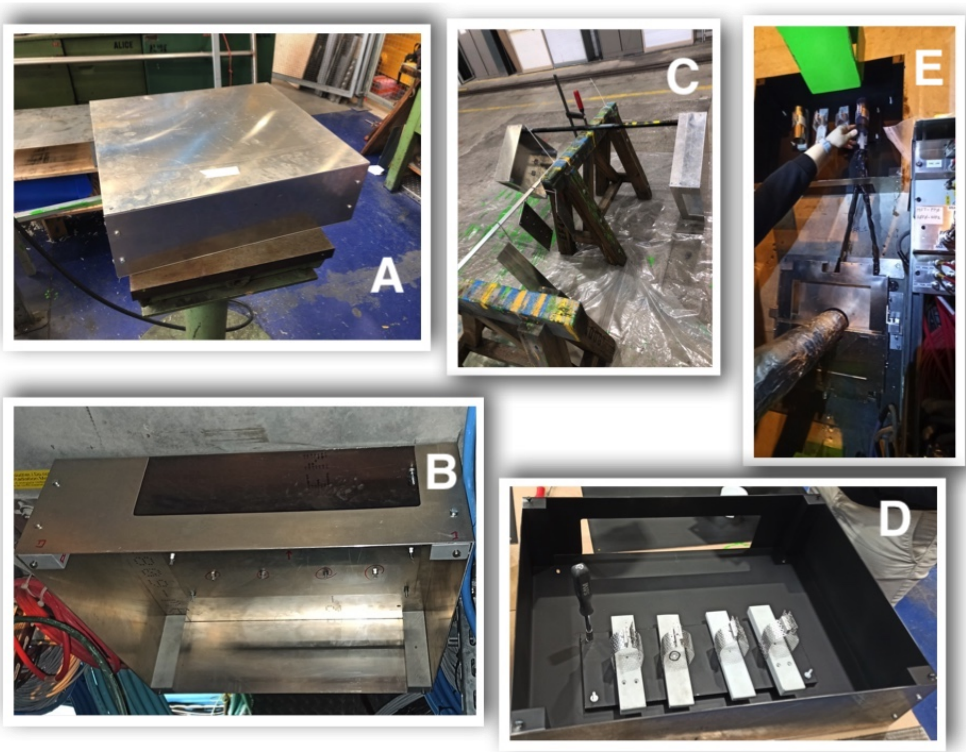

Figure 5.22: Pictures of the PMT-boxes construction: construction of the box (A), testing of the box on site (B), coating of the inner area with dark paint (C), prepared PMT box (D), testing of the finished box on site with optical fibres (E).

and D of Figure 5.22) to enhance the light insulation properties of the boxes. They were also equipped with PMT holders (see picture D of Figure 5.22), which keep the PMTs at a desired spot. After the construction, the boxes were tested on site under real conditions and with other parts of the detector to imitate the installation process (see pictures B and E of Figure 5.22).

5.7 Credits

Construction
Jesus Guillermo CONTRERAS NUNO
Tonatiuh GARCIA CHAVEZ
Gerardo HERRERA CORRAL
Tomas HERMAN
Evgeny KLASS
Katarina KRIZKOVA GAJDOSOVA
Diana KRUPOVA
Ildefonso LEON MONZON
Hector David REGULES MEDEL
Saul Anibal RODRIGUEZ RAMIREZ
Solangel ROJAS TORRES
Vojtech ZABLOUDIL

Logistics: Czech Republic
Zdenka CISLEROVA
Jesus Guillermo CONTRERAS NUNO
Solangel ROJAS TORRES
Vojtech ZABLOUDIL

Logistics: CERN
Arturo FERNANDEZ TELLEZ
Sergio PAISANO GUZMAN
Saul Anibal RODRIGUEZ RAMIREZ
Solangel ROJAS TORRES
Maciej SLUPECKI
Arturo TAURO
Wladyslaw Henryk TRZASKA
Vojtech ZABLOUDIL

Installation
Arturo FERNANDEZ TELLEZ
Tonatiuh GARCIA CHAVEZ
Pieter IJZERMANS
Hector David REGULES MEDEL
Saul Anibal RODRIGUEZ RAMIREZ
Solangel ROJAS TORRES
Maciej SLUPECKI
Wladyslaw Henryk TRZASKA
Vojtech ZABLOUDIL

Contributions form colleagues outside ALICE
Jan CEPILA
Petr CHALOUPKA
Janek CONTRERAS
Martin JANDA
Frantisek LOPOT
Martina LOPOTOVA
Libor SKODA

Chapter 6

Efficiency determination of the FDD photomultiplier tubes

The functionality of FDD relies heavily on the quality of the used PMTs and their operating voltage. The goal of the PMT characterisation is to check the performance of individual PMTs at different voltages and determine amplitude and charge gain curves. Twenty Hamamatsu H8409-70 photomultipliers were tested and characterised in order to choose the best 16 for installation.

It is important to note, that this measurement is just a pilot test to ensure the functionality of the PMTs and choose the best amongst them, as eventually, it is needed to re-do this characterisation after the whole system is installed and connected to the electronics and ready to operate. This enabled the opportunity to try various methods for the characterisation and make the choice of the PMTs in consideration of all of them.

The following methods were: illumination of the PMTs with low-intensity laser light, characterisation for minimum-ionisation particle (MIP) using cosmic muons and single photon calibration. The first two methods are further described in the following sections. There was an effort to perform the single photon calibration as well, but due to time limitations it was not possible to continue with the work and reach a satisfactory conclusion. However, the method is presented and described in Ref. [18], which also served as a base for our work.

6.1 Method 1: illumination with low-intensity laser light

The idea of the measurement is the following: the photomultiplier tubes are kept in a dark box and irradiated by low-intensity light while changing the voltage of the PMTs in order to get their characteristics with respect to the voltage. The produced signal is digitised and sent to the PC for further analysis.

The following components were used in the set-up:

- **Laser**

  A PicoQuant PDL 800-D laser driver and LDH-P-C-405 laser head were used in the set-up (see Figure 6.1). Its role was to provide the illumination light for the PMTs.

- **Pulse Generator (pulser)**

  A GW Instek AFG-3051 arbitrary waveform generator was used to fire the laser as well as to trigger the digitiser discussed below.

- **Photomultiplier tubes**

  A pair of photomultiplier tubes was used for the calibration. One was used for a reference, while the other was characterised. The characterised PMTs are Hamamatsu H8409-70 photomuliplier assemblies, their general properties were discussed in Chapter 4. The reference PMT is of the same model.

- **Digitiser**

  A CAEN V1742 digitiser (second from the left in Figure 6.2) was used to sample the signal from the PMTs. The used sampling rate was 5 GS/s (5 giga samples per second).

- **High voltage source**

  The photomultiplier tubes were powered by a HV source: the reference photomultiplier (labelled as Ref PMT in Figure 6.3) was fed by a constant voltage of 1300 V. The tested photomultiplier (labelled as FDD PMT in Figure 6.3) was fed by voltages varied from 1300 V to 2100 V to acquire the PMT gain with respect to the voltage.

- **VME bridge**

  As the digitiser uses the VMEbus protocol, a CAEN V1718 VME bridge (first from the left in Figure 6.2) is used to provide the communication with the PC, where the sampled raw data is stored.

Figure 6.1: Photo of the PDL 800-D laser driver and LDH-P-C-405 laser head, photo of the HV source (A), photo of the pulse generator (B).

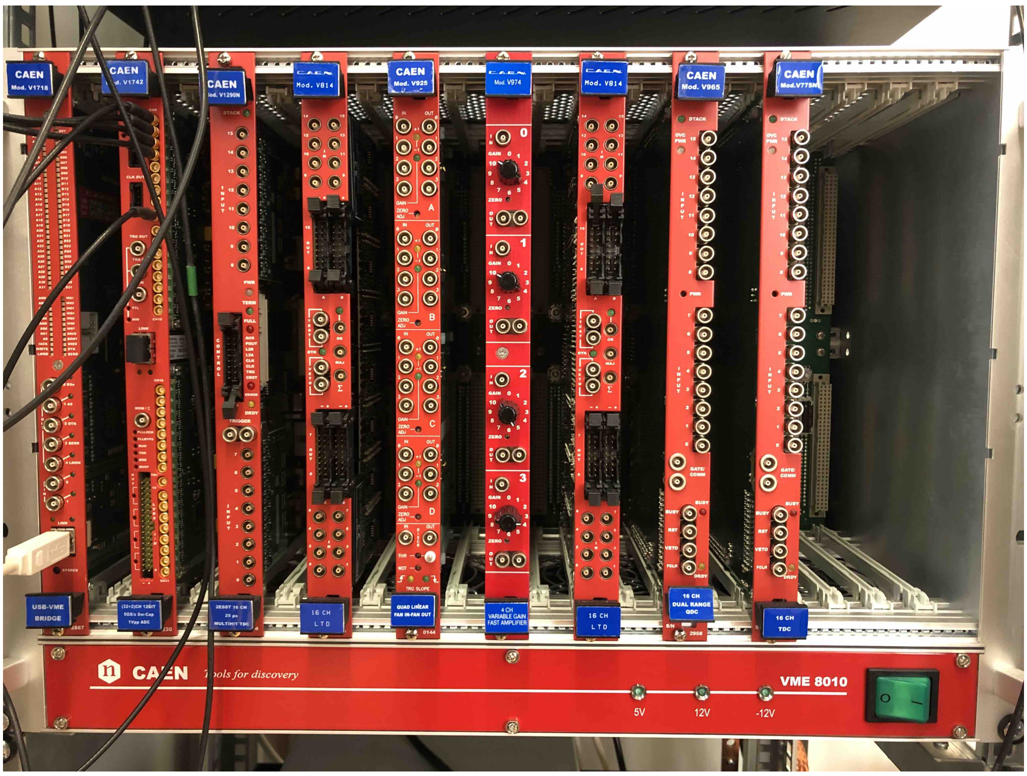

Figure 6.2: Photo of the CAEN VME crate used for the calibration. First from the left is V1718 VME bridge and second from the left is the CAEN V1742 digitiser. The rest of the components were not used in this measurement.

6.1.1 Set-up

The set-up used for the characterisation can be seen in Figure 6.3. The pulser triggers both the laser and digitiser. The light from the laser is attenuated with a mechanical attenuator to very low amplitudes. This light reflects off a sheet of paper, used as a reflective surface, and it is detected by the PMT photocathode. The PMT transforms the light into a corresponding electrical signal, which is further led to the triggered digitiser in order to be sampled. This data is sent to the PC, where it is stored for further analysis.

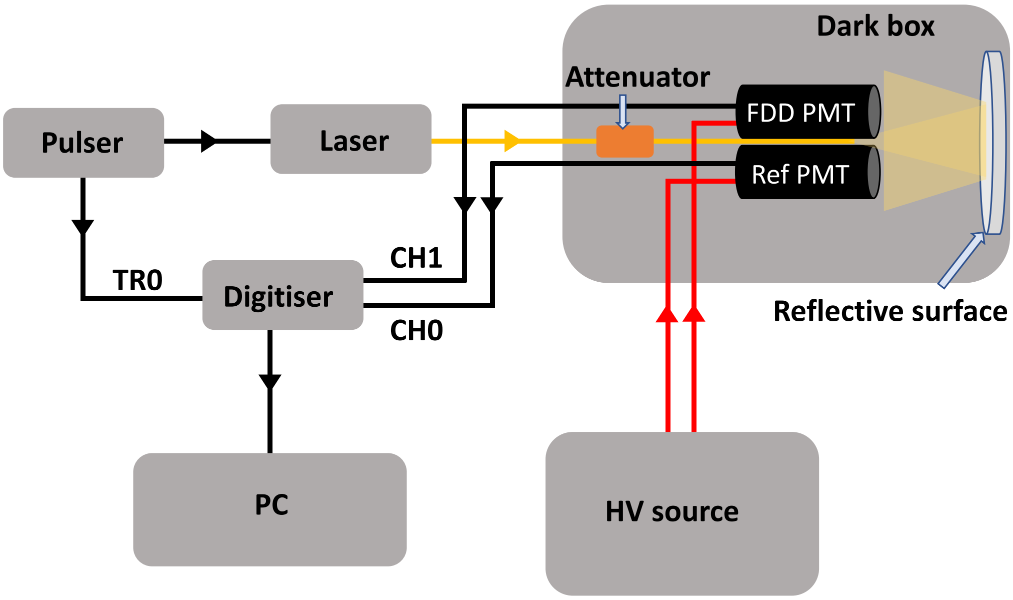

Figure 6.3: Scheme of the PMT calibration set-up.

6.1.2 Data collection and data set

The measurements were done with a pulser frequency of 1 kHz. A series of measurements was done individually for each tested PMT with the voltage ranging from 1300 V to 2100 V with a step of 100 V, while keeping the reference PMT at 1300 V. The measured property was the signal amplitude of the PMTs, which was sampled and saved to the PC. The laser intensity was kept constant throughout all of the measurements.

6.1.3 Data analysis

The FIT group developed a custom analysis program based on the CAEN digitiser readout application WaveDump which allows us to process the raw data. The program calculates many properties of the signal such as the time, amplitude or charge and it also produces their corresponding histograms.

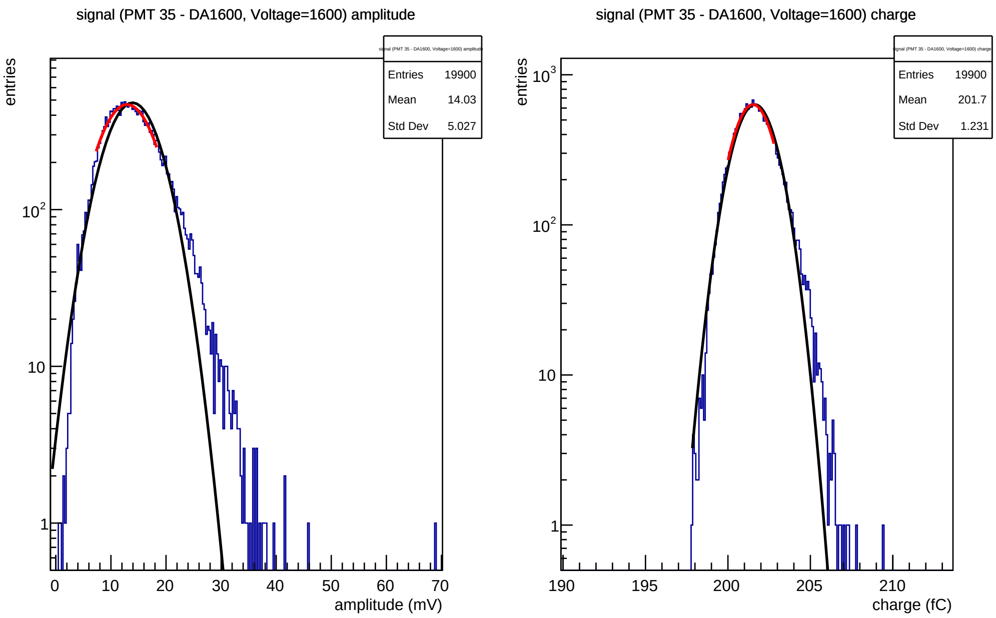

Figure 6.4: Amplitude and charge histograms of the signal for DA1600 at 1600 V.

The histograms for the amplitude and charge were fitted with a Gaussian distribution in order to obtain the mean of the signals in a restricted range. The fit was done with the ROOT framework [7]. A series of two Gaussian fits was used in order to acquire the best result. The first fit was used to roughly estimate the Gaussian parameters, which were set as the initial condition for the second fit. An illustrative example of the histograms and the fitting process is shown in Figure 6.4 and Figure 6.5.

Since there was an offset in the charge measurement, a pedestal run was used and its charge mean was subtracted from the signal. The pedestal run consisted of a measurement without the laser signal, which enabled to measure only the noise.

The amplitude and gain curves were obtained as a ratio of the amplitude and charge means of the tested PMT and the reference PMT. The data points were fitted with a power law. An illustrative example of the gain curves of a photomultiplier with serial number DA1586 is shown in Figure 6.6.

This method was a first try to do the PMT characterisation. At the time, it was an important way to get familiar with the set-up and the components, but the results were not utterly satisfactory. From the twenty PMTs that were tested, only six show the expected behaviour (proper gain curves of both amplitude and charge). This may have been due to the lack of experience, which may have caused problems in the data collection and the data analysis.

However, it was agreed on to proceed to another method and set-ups instead of trying to fix the mentioned problems as this set-up was suitable only for the measurement of a single PMT at a time. As this method is essentially different from the second method, the parameters of the gain curves cannot be compared directly with the

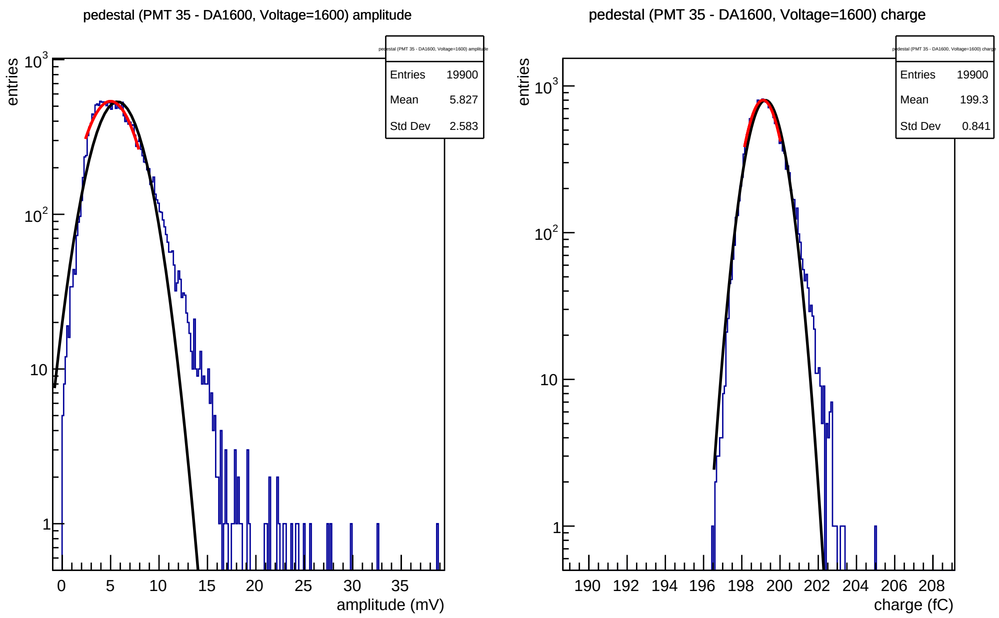

Figure 6.5: Amplitude and charge histograms of the pedestal for DA1600 at 1600 V.

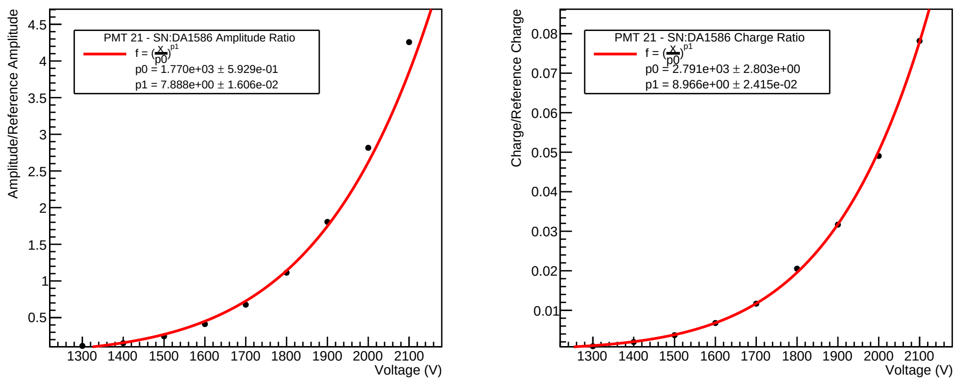

Figure 6.6: Plots of the amplitude and charge gain of DA1586.

parameters acquired from the second method.

In addition, the results are dependent on the particular settings of the set-up (laser intensity, choice of the reference PMT, etc.). This makes the method unsuitable to reproduction as the results are only on a relative scale amongst the set of the PMTs with a lack of set-up-independent value. This problem is solved in the other methods, which use minimum-ionising particles (MIP) or single photon detection.

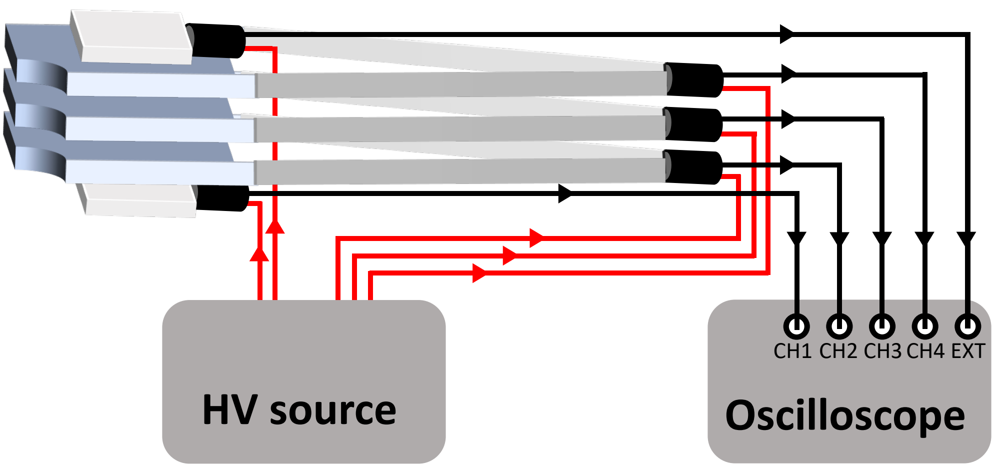

Figure 6.7: Scheme of the PMT calibration set-up with cosmic muons.

6.2 Method 2: cosmics

The second method uses cosmic muons, considered as minimum-ionising particles (MIP), which create a light signal in the scintillator pad. This light is then transferred to the PMTs. These are powered with different voltages in order to get the PMT characteristics.

6.2.1 Set-up

The set-up used for this measurement can be seen in Figure 6.7. It consists of three FDD modules, whose photomultiplier tubes are tested, and two scintillator triggers above and below the FDD modules, respectively. Each photomultiplier is powered by a high voltage source: the PMTs of the scintillator triggers are kept at a constant voltage, while the tested PMTs are fed by voltages of 1400 V, 1600 V, 1800 V, and 2000 V. The signal outputs are connected directly to the oscilloscope, which digitises the signal and calculates the peaks of the amplitude and charge as well as produces their corresponding histograms.

The oscilloscope (Teledyne Lecroy WaveRunner 8104, see Figure 6.8) allowed us to use the two scintillators (above and below the FDD modules) as a trigger. When they registered coincident signals above certain thresholds, the data from the tested PMTs was recorded. The trigger settings of the oscilloscope can be seen in Figure 6.9.

6.2.2 Data collection and data set

As the coincidence trigger affects the size of the data sample greatly, the measurement for each voltage of each run (batch of 3 PMTs) was performed for at least three hours in order to obtain a data set large enough. The main factors of this

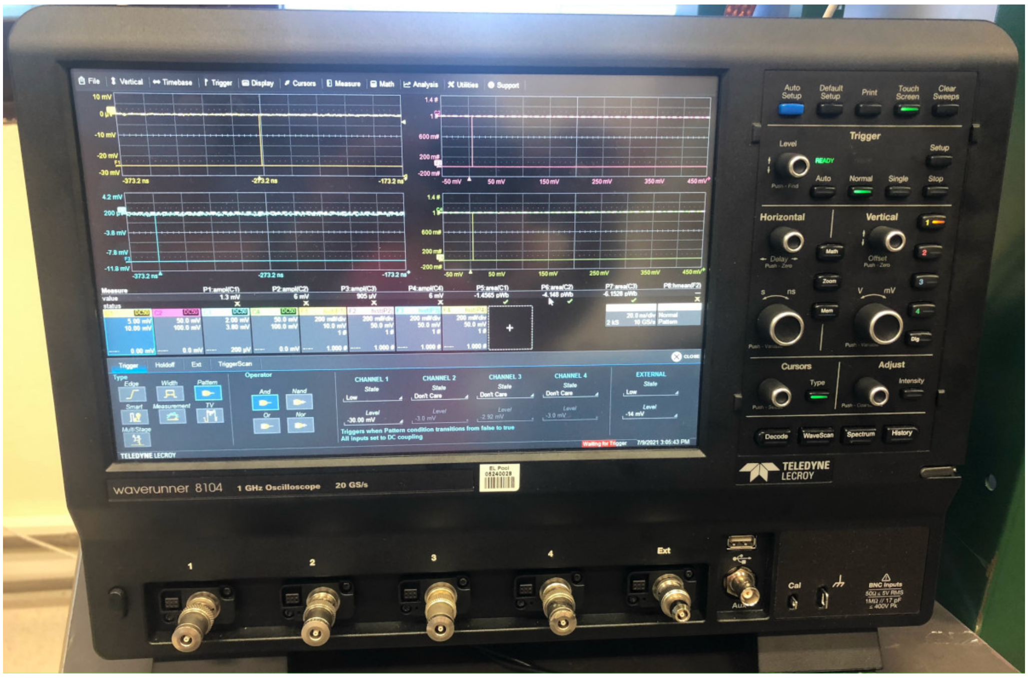

Figure 6.8: Teledyne Lecroy WaveRunner 8104 oscilloscope.

Figure 6.9: Trigger settings of the oscilloscope.

reduction were: the position of the trigger scintillators (resulting in triggering only the vertical muons), the size of the trigger scintillators (area less than half of the area of the FDD pads) and the thresholds for the scintillation triggers.

A series of eight measurements was done for each run: four of them with a different voltage for each measurement (1400 V, 1600 V, 1800 V, and 2000 V) and the coincidence trigger turned on, while the other four were done without the coincidence trigger in order to collect the background data. The latter four were used for the removal of the charge offset as mentioned in Method 1: illumination with low-intensity laser light.

The measured property was the signal amplitude of the three tested PMTs, out of which the oscilloscope calculated the charge. The histograms of amplitude and charge were saved together with the raw data of the amplitude. Nonetheless, only the histograms were used for the analysis, whereas the raw amplitude files served as a safety check in case of an error.

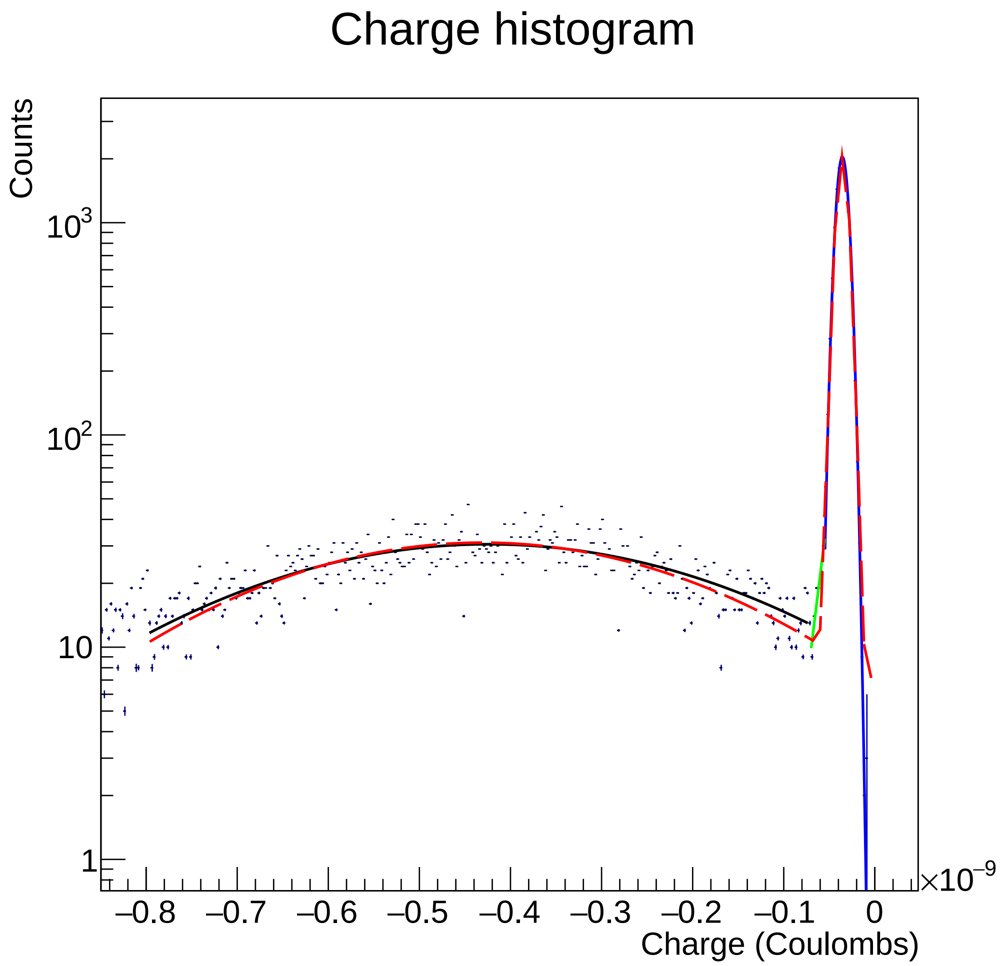

Figure 6.10: Fitting of the charge histogram. Black line represents a Gaussian fit of the signal, green line represents an exponential fit of the under-amplified electrons and blue line represents a Gaussian fit of the pedestal. All of these are combined in a fit represented by the red line.

6.2.3 Data analysis

The charge and amplitude histograms were fitted in three sub-ranges with three functions, which were then combined into one final fit. An example of the distribution is shown in Figure 6.10. The signal and the pedestal is fitted by a Gaussian function (black and blue colour in Figure 6.10, respectively), while the space between them is fitted by an exponential function (green colour in Figure 6.10). The choice of the ranges was done by hand for each histogram, as they were different for each PMT and voltage.

The mean and error of the Gaussian distribution (only of the signal for the amplitude, signal and pedestal for the charge) was saved to a file and it was later used for the gain curve. The pedestal charge was subtracted from the signal charge as in Method 1: illumination with low-intensity laser light. The amplitude and charge

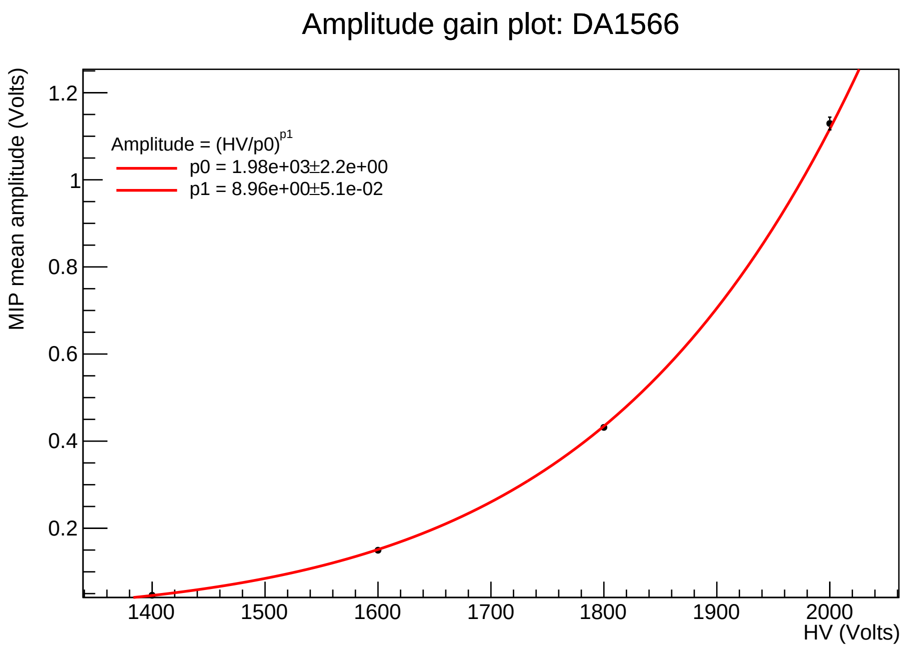

Figure 6.11: Plot of the amplitude gain curve of DA1566.

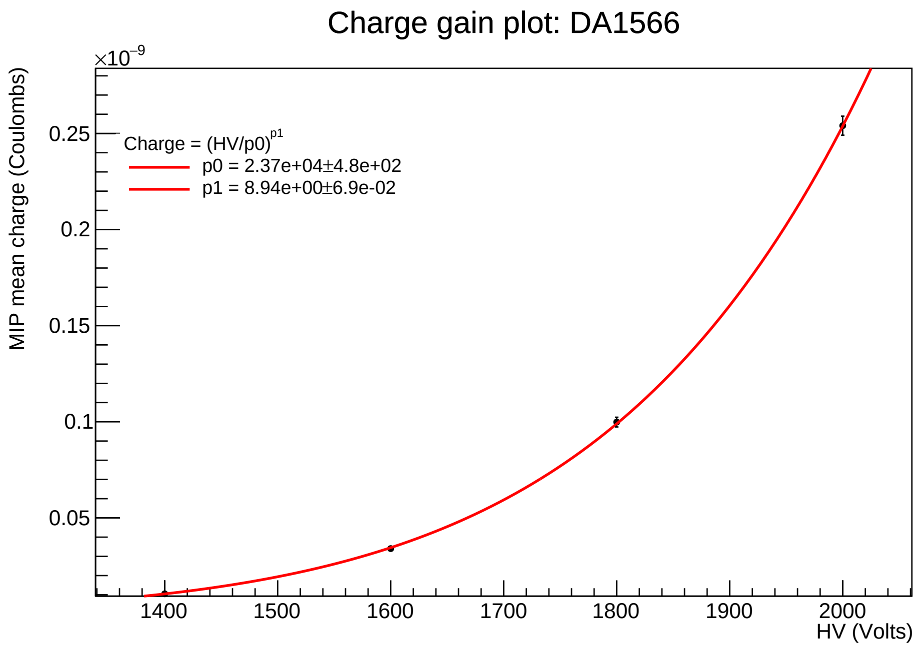

Figure 6.12: Plot of the charge gain curve of DA1566.

gain curves of PMT DA1566 are shown in Figure 6.11 and Figure 6.12, respectively. The data points were fitted with a power law as illustrated.

Table 6.1 shows the results of the data analysis. It contains the PMT serial number, the parameters of the amplitude and charge gain curves and the calculated high voltage corresponding to the amplitude of 8 mV/MIP (nominal HV).

Table 6.1: Table of the PMT characteristics

Serial Number	Ampl. p_0	Ampl. p_1	HV [V]	Charge p_0	Charge p_1
DA1550	2356 ± 9	8.5 ± 0.1	1331	33778 ± 2059	8.4 ± 0.2
DA1551	2566 ± 17	8.3 ± 0.1	1429	29480 ± 1146	9.1 ± 0.1
DA1555	2270 ± 6	8.9 ± 0.1	1316	28784 ± 686	8.7 ± 0.1
DA1562	2465 ± 2	9.0 ± 0.0	1441	37531 ± 321	8.3 ± 0.0
DA1563	2114 ± 7	8.6 ± 0.1	1205	33222 ± 1133	8.1 ± 0.1
DA1564	2229 ± 6	8.7 ± 0.1	1281	25716 ± 554	9.1 ± 0.1
DA1566	1976 ± 2	9.0 ± 0.1	1153	23670 ± 485	8.9 ± 0.1
DA1574	2694 ± 16	8.4 ± 0.1	1511	43020 ± 3106	8.2 ± 0.2
DA1577	3360 ± 53	6.4 ± 0.1	1586	65836 ± 5899	7.4 ± 0.2
DA1580	2439 ± 6	8.4 ± 0.1	1370	38611 ± 714	8.1 ± 0.0
DA1586	2799 ± 30	7.9 ± 0.2	1524	38944 ± 1724	8.5 ± 0.1
DA1587	2412 ± 11	8.7 ± 0.1	1384	29280 ± 1153	8.8 ± 0.1
DA1588	2641 ± 9	8.2 ± 0.1	1468	40434 ± 1149	8.2 ± 0.1
DA1592	3002 ± 4	7.7 ± 0.0	1602	44940 ± 379	8.2 ± 0.0
DA1593	2449 ± 11	8.4 ± 0.1	1374	39149 ± 1842	8.1 ± 0.1
DA1595	2778 ± 3	8.4 ± 0.0	1560	33947 ± 252	8.9 ± 0.0
DA1596	2416 ± 9	8.5 ± 0.1	1373	31815 ± 714	8.6 ± 0.1
DA1600	2477 ± 2	8.3 ± 0.0	1389	30697 ± 237	8.8 ± 0.0
DA1601	2585 ± 3	9.3 ± 0.0	1535	27680 ± 206	9.4 ± 0.0
DA1603	2491 ± 2	8.2 ± 0.0	1383	35038 ± 277	8.4 ± 0.0

Summary and outlook

This thesis provided the motivation for the ALICE upgrade for Runs 3 and 4 as well as the description of the newly added or upgraded elements. One of the new additions is the Fast Interaction Trigger (FIT), which will provide minimum-bias trigger for the detectors without continuous readout. One of the three FIT subsystems is the scintillation-based Forward Diffractive Detector (FDD), which is the main topic of this thesis.

The theoretical part of this thesis presents the introduction to particle physics and furthermore ultra-peripheral collisions (UPC). It explains the role of FDD in context of UPC and the other benefits that FDD incorporates. It also introduces the basics of scintillators and photomultiplier tubes, together with the description of the FDD components.

The main goal of this thesis was to construct the Forward Diffractive Detector. This was successfully finished and tested in order to prove that the detector is operational. This thesis provides detailed instructions for the construction of the detector parts and their assembly as well as the mention of the PMT efficiency determination.

It includes the installation of FDD-C, which took place in February 2021, and the preparation works for the installation of FDD-A.

Another important outcome of this thesis is the laboratory set-up at the Department of Physics at the Faculty of Nuclear Sciences and Physical Engineering (FNSPE) of the Czech Technical University (CTU) in Prague, where the FDD construction took place. This provides future possibilities to continue with work of similar character, mainly to explore the ways how to improve the current FDD design. Many ideas concerning the readout system such as different techniques for the light extraction from the plastic scintillator, testing different reflective surfaces such as full Mylar wrapping or a coverage with paint instead of aluminium foil are possible to be put to test. It is also intended to perform ageing tests of the plastic scintillators and the wavelength-shifting bars.

The next steps concerning the FDD will lead to the installation of FDD-A scheduled in July 2021 as well as connecting of FDD to all of the electronics. This will enable us to test the performance of the whole system together in order to prepare for pilot pp data-taking planned for October 2021.

Bibliography

[1] F. D. Aaron et al. “Combined measurement and QCD analysis of the inclusive e ± p scattering cross sections at HERA”. In: *Journal of High Energy Physics* 2010.1 (Jan. 2010). ISSN: 1029-8479. DOI: 10.1007/jhep01(2010)109. URL: http://dx.doi.org/10.1007/JHEP01(2010)109.

[2] M. Broz et al. “Performance of ALICE AD modules in the CERN PS test beam”. In: *Journal of Instrumentation* 16.01 (Jan. 2021), P01017–P01017. DOI: 10.1088/1748-0221/16/01/p01017. URL: https://doi.org/10.1088/1748-0221/16/01/p01017.

[3] The ALICE Collaboration et al. “The ALICE experiment at the CERN LHC”. In: *Journal of Instrumentation* 3.08 (Aug. 2008), S08002–S08002. DOI: 10.1088/1748-0221/3/08/s08002. URL: https://doi.org/10.1088/1748-0221/3/08/s08002.

[4] P Antonioli, A Kluge, and W Riegler. *Upgrade of the ALICE Readout & Trigger System*. Tech. rep. Sept. 2013. URL: https://cds.cern.ch/record/1603472.

[5] *BC-418, BC-420, BC-422 Premium Plastic Scintillators*. https://www.crystals.saint-gobain.com/sites/imdf.crystals.com/files/documents/bc418-420-422-data-sheet.pdf. Accessed: 2021-05-05.

[6] Michal Broz. *FIT long*. https://alice-figure.web.cern.ch/node/17251. Accessed: 2021-26-07.

[7] R. Brun and F. Rademakers. “ROOT: An object oriented data analysis framework”. In: *Nucl. Instrum. Meth. A* 389 (1997). Ed. by M. Werlen and D. Perret-Gallix, pp. 81–86. DOI: 10.1016/S0168-9002(97)00048-X.

[8] P Buncic, M Krzewicki, and P Vande Vyvre. *Technical Design Report for the Upgrade of the Online-Offline Computing System*. Tech. rep. Apr. 2015. URL: https://cds.cern.ch/record/2011297.

[9] Domenico Colella. *ALICE Inner Tracking System Upgrade: construction and commissioning*. https://arxiv.org/abs/1912.12188. 2019. arXiv: 1912.12188 [physics.ins-det].

[10] Hamamatsu Photonics K.K. Editorial Committee. *Photomultiplier tubes: Basics and Applications*. fourth. Hamamatsu Photonics K.K. Electron Tube Division, 2017.

[11] J. Contreras and Daniel Tapia Takaki. "Ultra-peripheral heavy-ion collisions at the LHC". In: *International Journal of Modern Physics A* 30 (Mar. 2015), p. 1542012. DOI: 10.1142/S0217751X15420129.

[12] Spencer R. Klein and Heikki Mäntysaari. "Imaging the nucleus with high-energy photons". In: *Nature Rev. Phys.* 1.11 (2019), pp. 662–674. DOI: 10.1038/s42254-019-0107-6. arXiv: 1910.10858 [hep-ex].

[13] Glenn F. Knoll. *Radiation Detection and Measurement, third edition*. New York: John Wiley and Sons, 2000. ISBN: 978-0-471-07338-3, 978-0-471-07338-3.

[14] Esma Mobs. "The CERN accelerator complex - 2019. Complexe des accélérateurs du CERN - 2019". In: (July 2019). General Photo. URL: https://cds.cern.ch/record/2684277.

[15] *Nanostructured organosilicon luminophores (NOLs)*. https://www.luminnotech.com/products/luminophores. Accessed: 2021-05-05.

[16] *Photomultiplier tube assembly H8409-70*. https://www.hamamatsu.com/eu/en/product/type/H8409-70/index.html. Accessed: 2021-10-06.

[17] *Photomultiplier tubes*. https://www.hamamatsu.com/resources/pdf/etd/PMT_TPMZ0002E.pdf. Accessed: 2021-07-07.

[18] R. Saldanha et al. "Model Independent Approach to the Single Photoelectron Calibration of Photomultiplier Tubes". In: *Nucl. Instrum. Meth. A* 863 (2017). Ed. by Guoqing Xiao, Hao Shen, and Guanghua Du, pp. 35–46. DOI: 10.1016/j.nima.2017.02.086. arXiv: 1602.03150 [physics.ins-det].

[19] Maciej Slupecki. "The Fast Interaction Trigger for the ALICE Upgrade". Presented 12 Jun 2020. PhD thesis. June 2020. URL: https://cds.cern.ch/record/2741462.

[20] Arturo Tauro. "ALICE Schematics". General Photo. May 2017. URL: https://cds.cern.ch/record/2263642.

[21] *Technical Design Report for the Muon Forward Tracker*. Tech. rep. Jan. 2015. URL: https://cds.cern.ch/record/1981898.

[22] *The Large Hadron Collider*. https://home.cern/science/accelerators/large-hadron-collider. Accessed: 2021-08-07.

[23] *Upgrade of the ALICE Time Projection Chamber*. Tech. rep. Oct. 2013. URL: https://cds.cern.ch/record/1622286.

[24] Chiara Zampolli. "ALICE data processing for Run 3 and Run 4 at the LHC". In: *PoS* ICHEP2020 (2021), p. 929. DOI: 10.22323/1.390.0929. arXiv: 2012.04391 [physics.ins-det].